Open Research Online

The Open University's repository of research publications
and other research outputs

Technology advancement of the CCD201-20 EMCCD for the WFIRST coronagraph instrument: sensor characterization and radiation damage

Journal Item

For guidance on citations see FAQs.

oro.open.ac.uk

Technology advancement of the CCD201-20 EMCCD for the WFIRST coronagraph instrument: sensor characterization and radiation damage

Leon K. Harding[1,a], Richard T. Demers[1,a], Michael Hoenk[a], Pavani Peddada[a], Bijan Nemati[a], Michael Cherng[a], Darren Michaels[a], Leo S. Neat[a], Anthony Loc[a], Nathan Bush[b], David Hall[b], Neil Murray[b], Jason Gow[b], Ross Burgon[b], Andrew Holland[b], Alice Reinheimer[c], Paul R. Jorden[d] and Douglas Jordan[d]

[a]Jet Propulsion Laboratory, California Institute of Technology, 4800 Oak Grove Drive, Pasadena 91109, CA, USA;
[b]Center for Electronic Imaging, Department of Physical Sciences, The Open University, Walton Hall, Milton Keynes, MK7 6AA, UK;
[c]e2v inc., 765 Sycamore Drive, Milpitas CA 95035, USA;
[d]e2v technologies, 106 Waterhouse Lane, Chelmsford, Essex, CM1 2QU, England

ABSTRACT

The Wide Field InfraRed Survey Telescope-Astrophysics Focused Telescope Asset (WFIRST-AFTA) mission is a 2.4-m class space telescope that will be used across a swath of astrophysical research domains. JPL will provide a high-contrast imaging coronagraph instrumentone of two major astronomical instruments. In order to achieve the low noise performance required to detect planets under extremely low flux conditions, the electron multiplying charge-coupled device (EMCCD) has been baselined for both of the coronagraph's sensorsthe imaging camera and integral field spectrograph. JPL has established an EMCCD test laboratory in order to advance EMCCD maturity to technology readiness level-6. This plan incorporates full sensor characterization, including read noise, dark current, and clock induced charge. In addition, by considering the unique challenges of the WFIRST space environment, degradation to the sensor's charge transfer efficiency will be assessed, as a result of damage from high-energy particles such as protons, electrons, and cosmic rays. Science-grade CCD201-20 EMCCDs have been irradiated to a proton fluence that reflects the projected WFIRST orbit. Performance degradation due to radiation displacement damage is reported, which is the first such study for a CCD201-20 that replicates the WFIRST conditions. In addition, techniques intended to identify and mitigate radiation-induced electron trapping, such as trap pumping, custom clocking, and thermal cycling, are discussed.

Keywords: electron multiplying charge-coupled devices; WFIRST-AFTA; radiation damage; L2 orbit; techniques: mitigation

1. INTRODUCTION

1.1 Wide Field InfraRed Survey Telescope–Astrophysics Focused Telescope Asset Coronagraph

The Wide Field InfraRed Survey Telescope–Astrophysics Focused Telescope Asset (WFIRST-AFTA) is a NASA space observatory that has been designed to probe dark energy, to carry out wide-field near infrared (NIR) surveys, and to discover and characterize extrasolar planets (hereafter exoplanets) in the visible spectrum. WFIRST-AFTA will make use of an existing 2.4-m aperture telescope and will advance what is currently possible in exoplanet spectral characterization and imaging. The telescope feeds an instrument suite consisting of a wide-field imager (WFI) and a coronagraph instrument (CGI). These two instruments are complementary. The

---

[1]Corresponding authors: Leon.K.Harding@jpl.nasa.gov; Richard.T.Demers@jpl.nasa.gov
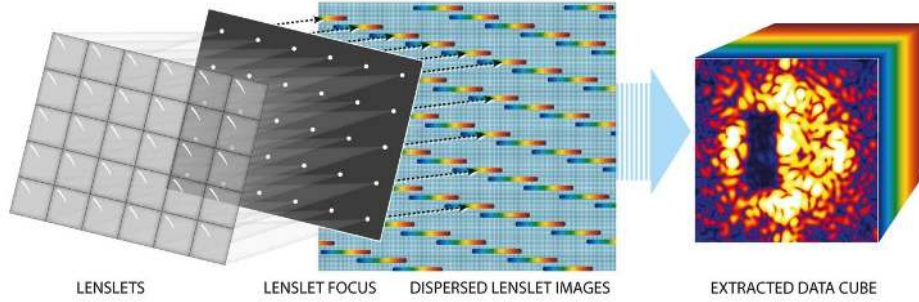
Figure 1. A lenslet array with a pinhole mask is clocked with respect to the rows of the electron multiplying charge-coupled device (EMCCD) in order to optimize the separation between neighboring spectra on the detector thereby reducing spectral crosstalk. A pinhole mask at the exit surface of the lenslet array serves to truncate the tails of the lenslet point-spread functions in order to reduce spectral crosstalk on the detector. A spectral data cube is extracted in postprocessing. Figure provided by Michael McElwain of Goddard Space Flight Center (GSFC).

WFI will collect NIR statistical data on planetary systems over large regions of the sky using gravitational microlensing, whereas the coronagraph will carry out direct imaging and detailed visible spectroscopy of a sample of exoplanets. The coronagraph will be able to detect and characterize cold Jupiters, mini-Neptunes, and possibly super-Earths[1] and for the first time directly image planets analogous to those in our solar system. This spectroscopic characterization will reveal the atmospheric composition of these planets and will be used to search for spectral signatures of life. In addition, the coronagraph will be used to characterize debris disks in and around planetary orbitsan important tool that can be used to improve our understanding of planet formation.

In order to adequately form images and collect spectra of exoplanets, it is necessary to suppress the starlight to a contrast of order 10^{-9} for cold Jupiters, mini-Neptunes, and super- Earths. The coronagraph accomplishes this by using (1) a series of masks to reject starlight, to block diffracted light, and to reduce starlight speckles, and (2) an adaptive optics system, employing a pair of deformable mirrors (DMs) in order to eliminate residual speckles due to optical imperfections in the entire optical beamtrain. The result is a high-contrast point-spread function (PSF) with a dark hole between inner and outer working angles allowing observations of faint companions.

The WFIRST-CGI can operate in two modes: (1) a hybrid Lyot coronagraph (HLC) for exoplanet photometry and discovery, and (2) a shaped pupil coronagraph (SPC) for exoplanet spectroscopy and debris disk characterization. The HLC uses a focal plane phase-amplitude mask, whereas the SPC uses a pupil mask with binary apodization. The flight instrument comprises a single optical beam train that will be operated in either the HLC or SPC mode. The CGI switches between the two operational configurations using active rotary mechanisms to change pupil masks, focal plane masks, Lyot masks, bandpass filters, and an actuated fold mirror to select either the imaging camera or the integral field spectrograph (IFS). In both the HLC and SPC modes, the pair of DMs is used for closed-loop reduction of speckle. This dual mode architecture enables the optimum coronagraph configuration to be used for the different types of planet/disk characterization. The two coronagraph architectures are complementary. The HLC can achieve deeper contrast at certain working angles, whereas the SPC is relatively insensitive to jitter and has lower chromaticity.

In order to maintain the contrast stability over observation times, a low-order wavefront sensor and control system in the coronagraph is used to sense and correct lower-order wavefront error resulting from (1) thermally-induced optical misalignment and optical surface distortions, and (2) line-of-sight (LOS) jitter caused by vibration sources, such as the spacecraft reaction wheels and the WFI cryocooler. A Zernike wavefront sensor uses the rejected starlight to sense aberrations from Z1,2 (x- and y-tilts) up to and including Z11 (spherical aberration). The x- and y-tilts resulting from LOS jitter are corrected using a fast steering mirror, whereas the low-order wavefront drifts are corrected by a pistoning fold mirror for focus correction and the DMs for other low-order aberrations, such as astigmatisms and comas.

When carrying out planet discovery, photometry, and disk imaging, the HLC or SPC relays an image of the high-contrast dark hole onto the imaging camera. A stationary polarizing beam splitter in front of the imaging

camera separates the dark hole image into two orthogonal polarizations, whose two resulting images fill a small rectangular area of the detector. When taking planetary spectra, by contrast, the IFS images a regular grid of spectrally dispersed PSFs onto the detector. Several aspects of the IFS design[2] further reduce the already very low-light level of the planet image from the coronagraph. The IFS separately collects spectra across the visible spectrum in three separately detected 18% wide sub-bands centered at 660, 770, and 890 nm. At the input of the IFS is a lenslet array used for spatial sampling the dark hole, where the PSF sampling on the lenslet array is 3×3 lenslets per D (PSF core). A two-element prism spectrally disperses the PSFs along a single axis, further spreading the light on the detector. Thus, the very low expected photon count requires subelectron read noise, dark current, and clock induced charge (CIC) to carry out planet spectroscopy. The formation of the grid of spectra on the detector is illustrated in Fig. 1.

1.2 WFIRST-CGI Detector Selection

1.2.1 Detector candidates

Many astronomical instruments have used conventional charge coupled devices (CCDs), segmented CCDs, or hybrid complementary metal oxide semiconductor (CMOS) focal plane arrays.[3–10] Conventional CCDs and hybrid VIS/IR CMOS[11, 12] devices have been the preferred focal plane arrays for both ground-based and space-based telescopes and visible/IR photometric instruments. Conventional CCDs have the advantage of being generally easier to characterize due to their extremely simple design. Older CCDs have less output taps and since noise increases with bandwidth, older CCDs have higher read noise. More recent CCDs have more output taps and are therefore less noisy and their primary source of noise is the output driver. The charge to voltage conversion in conventional CCDs occurs on the gate capacitor of a metal oxide semiconductor field-effect transistor (MOSFET) or junction gate field-effect transistor (JFET), which is inherently nonlinear, but if running high-power supply voltages with low-voltage signal swings, CCDs have linear response. In the design of CCDs, conversion gain, output driver strength, and bandwidth are linked and so design optimization is limited. Hybrid CMOS detectors, owing to their complex design, can be difficult to characterize but do not suffer from noise due to either charge transfer inefficiency (CTI) or CIC. The breed of CMOS sensors used in astronomy–typically source follower pixels–has high gain in the pixel and is therefore generally limited by pixel noise and insensitive to read noise in the column buffer. Source follower CMOS pixels typically use a gate capacitor with a MOSFET to convert charge to voltage and like CCDs are inherently nonlinear. Their response, however, is linear for most of the electron well range with nonlinearity for nearly empty and nearly full wells. In CMOS sensor design, the conversion gain, output driver strength, and bandwidth can be separately traded to optimize performance.

With the advent of the electron multiplying CCD (EMCCD) at the beginning of the last decade[13, 14] high signal to noise (S/N) performance became possible over much shorter timescales, resulting in negligible effective read noise and low spurious noise contribution. This performance is achieved by means of a multiplication register that lies after the conventional serial register where charge can be amplified by factors of thousands via avalanche multiplication. We explain this phenomenon in more detail in Sec. 2. In this sense, EMCCDs can outperform conventional CCDs and are technologically mature since they are produced in medium volume as a commercial product for medical devices and for ground-based observatory instruments. Nonetheless, EMCCDs have little or no space flight heritage.

In order to fully assess the S/N performance of the EMCCD and to compare with other candidate sensors having reasonably good performance but which may also have higher flight heritage and/or higher technological maturity, we carried out a trade study to compare the principal low-light level detector technologies. Following a survey of such detectors, candidate technologies were selected for this study. These candidates were evaluated and ranked based on (1) compliance with performance requirements for the Imager and IFS detectors, (2) flight heritage, (3) desired format and pixel pitch, and (4) planet yield predicted by a coronagraph model. The candidate detectors are [in order of descending technology readiness level (TRL)] scientific CCDs [Euclid, Hubble Space Telescope (HST) wide-field camera 3 (WFC3) and Gaia], Hybrid Visible Silicon Imager (JMAPS), EMCCDs, and scientific CMOS detectors. A brief description of each of these technologies is provided in this section and summarized in Table 1.

Table 1. Detector candidate technologies for JPL trade study. The read noise performances quoted are nominal values from respective studies that were released. The "Limitations" column refers to either a nonoptimal design detail for the WFIRST-CGI or to some test or study that has not yet been carried out. We note that at the time of the trade study, the CCD201-20 had not been radiation tested.

Short Name	Mission	Detector Model/N	Manuf.	TRL	Pixel (μm)	Full Format (pixel)	Limitations
sCMOS	Ground-based	CIS2051	Fairchild Imaging	4	6.5×6.5	2560×2560	Lowest TRL No rad./therm. cycling No temp data
Euclid CCD	Euclid vis. instrument	CCD273-84	e2v	6	12×12	4096×4096	RN ~ 3.5 e$^-$
HST CCD	HST WFC3	CCD43	e2v	9	15×15	2050×4096	RN ~ 3 e$^-$ Std epi depth
Gaia CCD	Gaia	CCD91-72	e2v	9	30×10	1966×4500	RN ~ 6 e$^-$ Unfavorable format
JMAPS HyViSI	JMAPS	HiViSI	Teledyne	6	18×18	1024×2048	RN ~ 5 e$^-$
EMCCD Std AN	WFIRST-CGI	CCD201-20	e2v	5	13×13	1024×2048	Low TRL No therm. cycling
EMCCD DD AN	WFIRST-CGI (DD)	CCD201-20	e2v	2	13×13	1024×2048	Thin epi (std)

Acronyms: TRL=Technology Readiness Level; RN=Read Noise.
HST=Hubble Space Telescope; WFC3=Wide Field Camera 3; DD=Deep Depletion.
Abbreviations: Std=Standard; AN=Analog; Rad./Therm. =Radiation/Thermal; pix=pixel.

i. Scientific CCDs: Scientific CCDs offer the highest TRL, having demonstrated excellent performance in multiple missions, including the HST wide-field and planetary camera 2, and WFC3 instruments, the Kepler focal plane, and the Gaia suite of instruments. A key advantage of scientific CCDs is the availability of a mature deep depletion (DD) technology, which is based on the use of high-purity silicon in the detector to enable high quantum efficiency (QE) in the 800- and 900-nm WFIRST-CGI bands. An important limitation of conventional scientific CCDs is the relatively high read noise, which is typically >2 e$^-$ pix^{-1}.

ii. Hybrid Visible Silicon Imager (HyViSI[TM]): Unlike CCDs, which require thousands of on-chip charge transfers to form an image based on serial readout by one or a few output amplifiers, CMOS detectors comprise two-dimensional pixel arrays with a photodiode and readout circuitry in each pixel. Teledyne imaging sensors have developed a hybrid silicon CMOS detector (the HyViSI detector[15]) by interconnecting a visible silicon photodiode array to a CMOS readout integrated circuit (ROIC). HyViSI hybrids combine the high responsivity of silicon photodiodes with CMOS parallel readout architecture, which provides unique capabilities. The correlated double sampling (CDS) read noise of HyViSI is comparable to that of scientific CCDs. The

Table 2. Detector candidate performance parameters for JPL trade study. We note that the excess noise factor, or ENF, is an added variance based on the EM process–this is explained further in Sec. 2. The read noise performances quoted are nominal values from commercial cameras, instrument reports, or measurements at JPL. We note that CIC can differ greatly for these devices based on their mode of operation as well as other factors. We measured nominal CIC for the CCD201-20 at 3×10^{-3} e$^-$ pix^{-1} fr^{-1}, and subsequently set all other applicable devices to this level as the best case for each. Dark current values stated correspond to nominal operating temperatures that are indicated in parentheses.

Performance Parameter	sCMOS	Euclid CCD	HST CCD	Gaia CCD	JMAPS HiViSI	EMCCD Std AN	EMCCD DD AN
ENF	1	1	1	1	1	1.41	1.41
CIC (e$^-$/pix/fr)	0	3×10^{-3}	3×10^{-3}	3×10^{-3}	0	3×10^{-3}	3×10^{-3}
I$_{dk}$ (e$^-$/pix/sec)	7×10^{-3} (233 K)	5.5×10^{-4} (153 K)	5.5×10^{-4} (190 K)	1×10^{-3} (158 K)	1×10^{-3} (170 K)	3×10^{-5} (165 K)	5×10^{-4} (165 K)
RN (e$^-$)	1.5	3.6	3.1	4.6	5	0.2[†]	0.2[†]
QE, 550 nm (%)	55	83	63	90	84	92	92
QE, 660 nm (%)	52	83	65	89	89	90	90
QE, 890 nm (%)	12	40	25	24	85	27	53

[†]Using Electron Multiplication (EM) gain of ∼450 based on an output amplifier read noise of 89.78 e$^-$ at a 10 MHz read out rate (see Table 7).

nondestructive parallel read capability of the CMOS ROIC enables reduction of the standard CDS read noise by recording multiple reads during integration (a.k.a. Fowler sampling or sampling up the ramp, SUTR) and fitting the results to a linear ramp. Such techniques are widely used in astronomy to reduce the contribution of reset and read noise. In addition, nondestructive read capability enables easy and accurate removal of cosmic rays (CRs) while preserving signal. Finally, since HyViSI detectors do not transfer charge through many pixels, they are not susceptible to deferred charge, which is one of the main limitations of scientific CCDs exposed to high radiation environments. HyViSI detectors were hybridized to the H4RG-10 ROIC for the U.S. Navy under the Joint Milli-Arcsecond Pathfinder Survey (JMAPS) program.[16] Although the JMAPS mission was canceled before launch, the H4RG-10 HyViSI flight detectors attained TRL-6 status.

iii. Electron Multiplying CCDs (EMCCDs): EMCCDs are a variant of scientific CCDs, in which a specially designed serial output register provides amplification using avalanche multiplication of collected charge. Charge amplification in EMCCDs significantly improves low-light level sensitivity by effectively suppressing read noise by many orders of magnitude [depending on the electron multiplication (EM) gain]. Although EMCCDs are less mature than scientific CCDs, e2v manufactures EMCCDs using the same materials, designs, and processes developed for high-heritage scientific CCDs. Some devices contain important design variations relevant to the space environment; however, the CCD201-20 (see Table 1) is not made with e2v's radiation-hard oxide
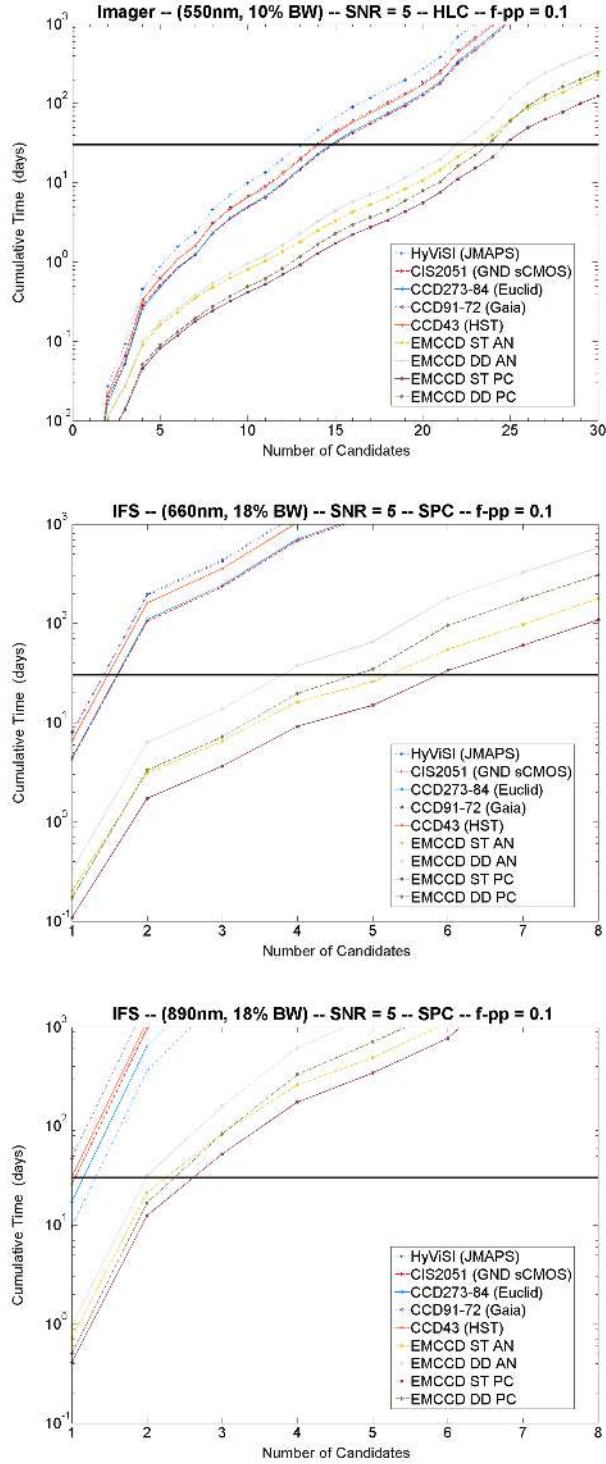
Figure 2. Analytical prediction of observation time required to achieve S/N = 5 versus the number of planets for each of the detector candidates. (a) 550-nm 10% Imager band (HLC), (b) 660-nm IFS 18% band (SPC), and (c) 890-nm IFS 18% band (SPC). f-pp denotes the postprocessing residual error and is assumed to have a value of 0.1 consistent with contrast improvement (reduction) of a factor of 10. The horizontal black line indicates a 30-day threshold.

process (see Sec. 4.2.1 for further discussion). EMCCDs have undergone extensive development and testing for ground-based astronomical instruments and medical applications. One EMCCD has been tested in radiation environments[17] comparable to the planned WFIRST orbit. e2v can provide customized DD EMCCDs, enabling high QE in the 800- to 980-nm band. However, DD EMCCDs are less mature than DD conventional scientific CCDs. Unlike the latter, DD EMCCDs require a special front-side implant. Additionally, DD CCDs and EMCCDs are incompatible with bias voltages required for inverted mode operation (IMO). Consequently, DD EMCCDs must be operated in noninverted mode operation (NIMO), which results in far higher surface dark current, the dominant contributor to dark current.

iv. Monolithic CMOS detectors: Until relatively recently, monolithic visible CMOS detectors were too noisy to compete with CCDs in low-light level imaging applications. However, advances in scientific CMOS detector design and fabrication led to the development of CMOS detectors with subelectron read noise. In 2009, Fairchild Imaging teamed with Andor Technology and PCO AG to develop a commercially available line of scientific monolithic CMOS detectors and cameras that are competitive with EMCCDs in low-light level imaging applications. Monolithic CMOS detectors have all of the advantages offered by parallel read architecture, as described nearby for the HyViSI CMOS detectors.

1.2.2 Detector trade study

The trade study was composed of seven specific detector models from four competing technologies. The seven candidates were as follows:

1) Monolithic scientific CMOS.

2) Conventional CCDs as used in EUCLID's visible focal plane array.

3) Conventional CCDs as used in HST's WFC3.

4) DD CCDs as used in Gaia's large Astrometric Focal Plane (AFP[18]).

5) Hybrid Silicon CMOS arrays as used in the JMAPS focal plane array.

6) Standard silicon-thickness EMCCD operated in analog EM gain mode and photon counting mode.

7) DD EMCCD operated in analog EM gain mode and photon counting mode.

To evaluate the relative science yield of the candidate detectors, we simulated end-to-end CGI performance using each of seven specific detector candidates. The model predicted the time required to collect images and spectra of planets from a list of known radial velocity (RV) planets. The predicted observation time was calculated as the time required to achieve a SN of 5 for either planet imaging or spectroscopy. The performance parameters that were used as model inputs appear in Table 2. All parameters were taken from available literature or from measurements collected by the authors (Fairchild Imaging CIS2051 specifications sheet, Endicott et al. 2012,[19] Kimble et al. 2009,[20] Prod'homme et al. 2011,[21] Gaume et al. 2009,[16] this work). For ease of analysis, all CCDs were assumed to have the same value for CIC, though in reality CIC between different CCDs can vary an order of magnitude depending on whether they are operated in NIMO or IMO, as well as pixel size, clock voltages, and operating speed. However, CIC measurements for many of the CCD candidates did not exist because it is not the leading contributor to overall S/N. Our assumption of the same CIC for all of the CCD candidates represents a best case for each. We find in the end that this assumption does not impact the final result. In addition to the seven candidates listed previously, the model included simulation of both the standard thickness and DD EMCCD as operated in photon-counting mode. Thus, a total of nine different cases were analyzed using the model. The underlying model assumptions are as follows:

7

Table 3. Detector trade matrix showing 12 discriminator categories, labeled a to l. Each option was separately scored against each discriminator. The scores were categorized as follows: Best (best performance), Wash (indistinguishable from Best), Small (lower performance but small difference from Best), Sig (lower performance but significant difference from Best), and Very lg (lower performance but very large difference from Best). These rankings were assigned numerical scores (Best = 4, Wash = 4, Small = 3, Sig = 2, Very lg = 1).

Decision Statement: Select a detector model for the flight IFS camera.

ID	Discriminator	Weights (%)	Option 1 sCMOS	Option 2 Euclid CCD	Option 3 HST CCD (WFC3)	Option 4 Gaia CCD	Option 5 JMAPS HiViSI	Option 6 EMCCD AN	Option 7 EMCCD DD AN
a	RN<0.2 e$^-$/pix	6	Sig	Very lg	Very lg	Very lg	Very lg	Wash	Best
b	CIC< 3×10^{-3} e$^-$/pix/fr	5	Best	Wash	Wash	Wash	Wash	Wash	Wash
c	$L_{dk} < 5 \times 10^{-4}$ e$^-$/pix/sec	5	Sig	Sig	Sig	Very lg	Sig	Best	Sig
d	QE, 550 nm	5	Very lg	Small	Very lg	Wash	Very lg	Wash	Best
e	QE, 660 nm	5	Very lg	Small	Very lg	Sig	Best	Sig	Wash
f	QE, 890 nm	5	Very lg	Very lg	Very lg	Very lg	Best	Very lg	Very lg
g	Reach TRL 6 (July 2016)	20	Sig	Best	Wash	Wash	Wash	Sig	Very lg
h	Format: 1024 × 1024 (min)	3	Wash	Wash	Wash	Wash	Wash	Wash	Best
i	Pixel pitch (sq): 13 – 15 μm	3	Sig	Small	Wash	Sig	Small	Best	Wash
j	# planets imaged (30 dys) (Imager, 550 nm)	15	Very lg	Very lg	Very lg	Very lg	Very lg	Best	Wash
k	# planets spectrally char. (30 dys, IFS, 660 nm)	14	Very lg	Very lg	Very lg	Very lg	Very lg	Best	Sig
l	# planets spectrally char. (30 dys, IFS, 890 nm)	14	Small	Small	Small	Small	Small	Best	Wash
	Weighted Sum	**100**	**1.9**	**2.4**	**2.3**	**2.4**	**2.5**	**3.4**	**2.9**

Table 4. Evaluation of detector risks and opportunities.

ID	Descrip.	Option 1 sCMOS	Option 2 Euclid CCD	Option 3 HST CCD (WFC3)	Option 4 Gaia CCD	Option 5 JMAPS HiViSI	Option 6 EMCCD AN	Option 7 EMCCD DD AN
LIKELIHOOD								
Risk 1	Low yield/ failed lot	Low	Low	Low	Low	Low	Low	Medium
Risk 2	Low operability	Low	Low	Low	Low	Low	Low	Medium
Risk 3	Radiation degradation (EOL)	Low	Medium	Medium	Medium	Medium	Medium	Medium
Opportunity 1	Science discovery	Low	Low	Low	Medium	Medium	High	High

1) HLC design version of January 2014; this HLC design has similar contrast in working angles to the current HLC design. The coronagraph focal plane mask design in the 2014 HLC design was not easy to fabricate. The current version mask design is easily fabricated. This does not affect the detector comparison.

2) SPC design version of December 2013.

3) Exoplanet detection targets were taken from a known list of RV planets sorted for the model in order of increasing difficulty of detection, as measured by the time required to achieve S/N of 5.

4) The exoplanet zodiacal background is the same as the local zodiacal background, i.e. 22 mag arcsec^{-2}.

5) A factor of 10 improvements in contrast results from data postprocessing. The postprocessing factor, f-pp, is assumed to have a value of 0.1 consistent with contrast improvement (reduction) of a factor of 10. This is the largest single contributor to the model uncertainty but this uncertainty affects all candidates equally.

The analytical model predictions of planet yield are shown in Fig. 2. The model showed that for the expected science targets, the IFS detector will sense a mean signal on the order of 3×10^{-3} e$^-$ pix^{-1} sec^{-1}. The target planets would be imaged using the imaging camera and would be spectrally characterized in each of the three IFS bands in the presence of stellar zodiacal background and detector noise. In Fig. 2, the model results are shown separately for the imaging channel fed by the HLC and for the two of the three IFS spectral bands that are fed by the SPC. The imaging channel uses a 10% spectral band centered at 550 nm, whereas the two analyzed IFS bands are centered at 660 and 890 nm, each with 18% spectral bandwidth. It is seen from the analytical results that among the seven trade study candidates, both the standard thickness and DD EMCCD outperformed all the other detector candidates in each of the three observational cases, regardless of whether the EMCCD was operated with analog gain or in photon-counting mode. In each case, the best performer was the standard thickness EMCCD in photon-counting mode. There is a significant performance gap between the four EMCCD variants and the other five detectors, whose performance was quite similar. For the WFIRST-CGI, the EMCCD has the best overall performance.

For the selection of the baseline CGI flight detector, the seven candidates were scored separately in 12 discriminator categories: six device performance parameters, flight heritage (TRL), pixel size, array format, and the science yield as measured by number of planets detected in 30 days in each of three channels. All of these discriminator scores were weighted and summed for an overall score. The highest weighted discriminators were (1) flight heritage (ability to reach TRL-6 by July 2016), weighted at 20% and (2) the time required to image and spectrally characterize planet targets, weighted at 43%. The highest scoring candidate was the DD EMCCD followed by the standard thickness EMCCD. The scoring with weights and summary scores are tabulated in Table 3. The EMCCD outperforms the other candidates because of its superior S/N at CGI photon flux levels, largely due to the order of magnitude reduction in read noise resulting from avalanche charge multiplication. The standard thickness EMCCD scored highest, followed by the DD EMCCD. The next lowest scores correspond to the three conventional CCDs and the HyViSI CMOS detector. The scoring differences within this subgroup are not deemed significant. The lowest score belongs to the monolithic CMOS detector. Commercially available scientific monolithic CMOS detectors have low QE in the 890-nm band. This is not a fundamental limit of monolithic CMOS technology. The QE of CMOS is fundamentally limited by the optical properties of silicon and the thickness of the absorbing layer.

The seven detector candidates were also evaluated in relation to risks and opportunities, as shown in Table 4. The standard thickness EMCCD was assessed to have manageable risk with high opportunity in science yield. The DD EMCCD offers one performance advantage over the standard thickness version. As shown in Table 2, the QE for the DD device is higher in the 770- and 890-nm bands. However, e2v has never fabricated the CCD201-20 with DD silicon and therefore, selection of this device would entail risks of low fabrication yield or low device operability. Additionally, a DD device cannot be run in IMO; therefore, dark current contribution is significantly higher and far outweighs the benefit of greater QE response in the NIR, consistent with the predictions in Fig. 2. (We discuss this in more detail in Secs. 5.3 and 5.5.3.) The standard thickness version of CCD201-20 is a standard product fabricated in medium volume for commercial applications and therefore has well characterized yield and low fabrication process risk. As a result of this evaluation process, the selection of the EMCCD as the imaging and IFS flight detector stands on firm ground.

1.3 Detector Technology Development Plan

Under NASA prephase-A technology development funding, JPL is moving forward the technological maturity of the CCD201-20 for space flight in order to reach NASA TRL-6. A three-part program to advance the device maturity is under way, consisting of (1) radiation environment testing, (2) noise performance optimization, and (3) thermal environment testing.

1.3.1 Radiation environment testing

Phase I: In the first of a two-phase radiation test, the radiation hardness of a pair of CCD201-20 engineering grade devices at ambient temperature was characterized after having been irradiated by a single exposure displacement damage dose (DDD) representative of a 6-year mission with direct insertion to L2 orbit. The result is also relevant to a potential geosynchronous orbit, as explained in Sec. 3. This first phase was carried out to provide an early indication of survivability of the CCD201-20 in the L2 radiation environment since no EMCCD has yet been qualified or flown in space and, as mentioned previously, a large format EMCCD of this design has not yet been radiation tested. The results of phase I are relevant to a mission in which periodic warm cycling of the coronagraph EMCCDs would be conducted to reverse some of the radiation-induced damage. The results of phase I are presented in Sec. 6.

Phase II: For the second phase of radiation testing, the CCD201-20 will remain operational and will be maintained at cold operating temperature ($-108°$ C; $\sim$165K) while being subjected to multiple DDDs with a cumulative dose equal to the 6-year mission life at L2. The device performance will be characterized before and after four separate proton doses in order to provide information on the rate of performance degradation throughout the 6-year lifetime. The results of phase II testing will provide a worst-case test of radiation hardness, representing flight operation over 6 years without the benefit of in-flight warm cycling or any longer term annealing that may occur over time at this colder temperature.

We note that although Michaelis et al.[17] carried out a DDD study of the CCD201-20, the device was operated at 5 frames per second for signal levels of 10 e$^-$, with multiplication gain of 100. Since the effects of radiation can greatly affect a device in different ways based on its operating conditions (discussed later in Sec. 6), we conducted the phase I study as a survivability test for the CCD201-20 specifically for the WFIRST-CGI. Therefore, the sensor was run under higher gain conditions (by a factor of 2), for both high flux (>1600 e$^-$) and low flux ($\sim$8 e$^-$) signals, and for an integration times of 100 s. This test plan was important based on the disparate operating modes of the CGI. In phase II, the CCD201-20 will be irradiated over the full range of proton fluences reflecting beginning of life (BOL) to end of life (EOL) for L2, while kept at cryogenic temperatures in the beamline, where the device will be under power at all times in order to measure flat-band shifts as expected in flight. This will be the first time that a CCD201-20 is subjected to this kind of radiation test.

1.3.2 Performance optimization

Proton radiation results in the creation of charge traps, which reduce the EMCCD charge transfer efficiency (CTE). The CTE can also be written as 1$-$CTI, which is the "charge transfer inefficiency". We will use the CTI term for discussion of this phenomenon for the remainder of this paper. Techniques such as pocket pumping[22-28] will be used to characterize the traps in the postirradiation EMCCDs. Once characterized, various operational mitigation techniques, such as charge injection, and various clock waveforms will be used to optimize the performance in the presence of charge traps.[29] In addition, postprocessing correction algorithms[30] will be tested.

1.3.3 Thermal environment testing

The CCD201-20 will undergo multiple thermal cycles spanning the mission survival temperature range and the resulting performance degradation will be characterized. A device will also undergo a 24-h thermal soak at the warm and cold survival temperature extrema.

2. ELECTRON MULTIPLYING CCDS AND THE CCD201-20

The introduction of the EMCCD[13,14] enabled subelectron effective read noise performance over a wide range of readout rates. Its architecture is very similar to that of a conventional CCD. The difference lies in the EMCCD's so-called high-gain or EM register. This is an extended multiplication stage containing a large-signal output that lies after the conventional serial register. In this region, electrons can be amplified by a process known as avalanche multiplication, in which high-voltage clocks produce electric fields in the silicon that are high enough to amplify charge via impact ionization. Crucially, this process is inherently stochastic, where there is $\sim 1-1.5\%$ probability of an extra electron getting generated per electron per given multiplication stage. Since a device can contain hundreds of multiplication stages, the probability of amplification becomes significant, and the subsequent EM gain, G, can amplify the signal by factors of thousands:

$$G = (1 + \alpha)^N,\tag{1}$$

where α is the $\sim 1 - 1.5\%$ probability of amplification and N is the number of stages. The result is a much higher S/N, albeit at the proportional reduction in pixel charge handling capacity. It is important not to continuously saturate the device under high amplification, since this can reduce the lifetime of the EM register. We note that there is an added variance in the EM output that consequently reduces the S/N, which results in an effective reduction of the sensor's QE by up to $\sim$50%. This is referred to as the "excess noise factor" (ENF); however, post-readout techniques can reclaim this reduction in QE.[31] The ENF can be calculated as follows:

$$ENF^2 = \frac{\sigma_{op}^2}{(G)^2 \cdot \sigma_{ip}^2},\tag{2}$$

where σ_{op}^2 is the variance in the output and σ_{in}^2 is the variance in the input (Robbins & Hadwin 2003[32]). The ENF asymptotically approaches $\sqrt{2}$ for gains $\geq$10, as shown:
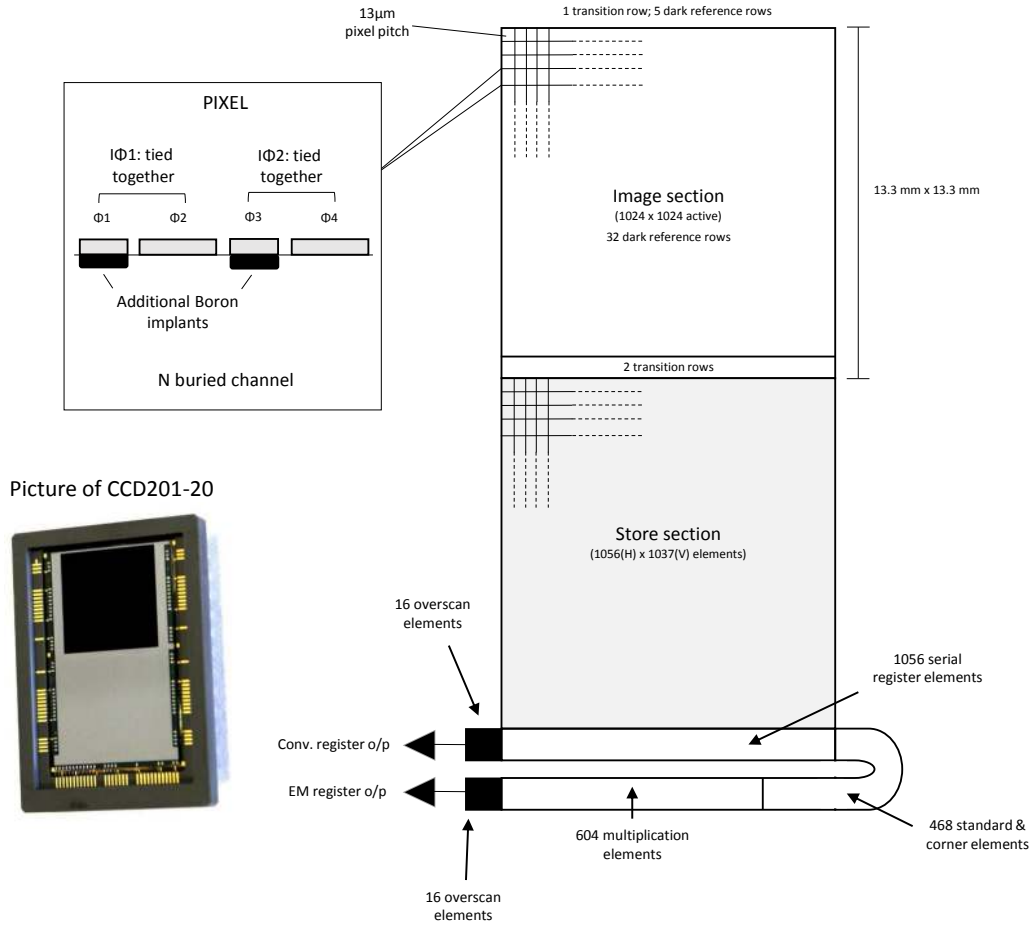
Figure 3. Schematic of CCD201-20. Charge is passed from the image section to the store section and subsequently read out through either the conventional or EM registers. To the left, we also include the approximate configuration of the two-phase boron implants within a pixel, where the image and store sections have an identical design. Electrode pairings, as indicated, is employed for standard clocking. Adapted from the e2v CCD201-20 specifications sheet.

$$ENF^2 = \frac{2}{\alpha + 1}, \tag{3}$$

because $\alpha << G$. This is the theoretical limit of the noise floor.

The high gain amplifier is driven by much higher voltages (>40 V) than the conventional register ($\sim$11 V) and can deliver an effective read noise of <<1 e$^-$ rms with EM gain, whereas the conventional amplifier provides a typical noise of $\sim 3 - 10$ e$^-$ rms. Importantly, as a result of much higher bias voltages applied via the high-voltage clock (that directly controls the gain), relatively low amounts of raw signal can quickly lead to saturation of pixels in the high-gain register. Therefore, there is always a tradeoff between the desired reduction in read noise and a reduction in the effective pixel charge capacity in order to achieve the highest S/N yield. Indeed, the employment of high gain at low temperatures (less than approximately < -90° C) can also affect a sensor's CTI, which is discussed later in Sec. 6. Thermal stability in the CCD controller is extremely important, since the gain will remain fixed for a fixed CCD temperature, T but will strongly vary as a function of δT but also for changing bias voltage conditions. All of these factors, in addition to those discussed later in this document, must

Table 5. Specifications of the CCD201-20 EMCCD, from e2v.

Parameter	Specification
Sensor family	EMCCD
Variant	BI*, 2-Phase
Active pixels (image)	1024 (H) × 1024 (V)
Frame Transfer (store)	1056 (H) × 1037 (V)
Image area	13.3 mm × 13.3 mm
Pixel pitch	13 μm
Active area CHP†	80,000 e$^-$ pix^{-1}
Gain register CHP†	730,000 e$^-$ pix^{-1}
Fill factor	100%
# O/P amplifiers	1 × Conv., 1 × EM
Multiplication elements	604
Dark reference columns	32
Overscan elements	16

*BI = Back-Illuminated; †CHP = charge handling capacity.

be heavily considered when optimizing an EMCCD for low-flux observing. By considering the high dynamic range provided by the conventional amplifier and the high sensitivity provided by the EM amplifier, EMCCDs are placed as an ideal detector for many astrophysical applications, including the WFIRST-CGI.

As previously outlined in Sec. 1.2, the CCD201-20 sensor (hereafter CCD201) has been baselined for the CGI, for both the Imager and the IFS. Although development of a ∼4K × 4K EMCCD is under way (the e2v CCD282), it is still at the early stages of testing,[33] thus making the CCD201 the largest-format EMCCD device currently available from e2v. It is a two-phase, frame transfer sensor, and has dual output amplifiers, as outlined in Table 5 and shown in Fig. 3. Even though the CCD201 is designed to be operated as a two phase CCD, four-phase clocking is possible because each of the parallel clocking lines are connected to a separate pin on the package; however, e2v has included two boron implants under phases $\phi 1$ and $\phi 3$, thus facilitating IMO, which, in addition to deep sensor cooling, further suppresses contribution from minority carriers from thermal generation, namely surface dark current. We have used this capability for four-phase clocking of the CCD201 in order to use the trap pumping technique[22] to characterize radiation-induced traps (see Sec. 6.3). All of the results that are outlined in this paper were carried out with standard back-illuminated silicon CCD201s, which have an image section of 1024 × 1024 active pixels with a store section of 1056 × 1037 pixels, see Fig. 3. Thinning and back-illumination help to improve QE, which peaks at >90% at 550 nm (we currently use the standard midband e2v coating.[48] The CCD201 can demonstrate a maximum well depth of 80,000 e$^-$ in the image section and 730,000 e$^-$ in the gain register. Pixels in the gain register are designed to have a large full well capacity (FWC) in order to avoid saturation during readout. The full spectral range (>15% QE transmission) of the sensor lies between ∼ 300 − 1000 nm, allowing tests in all of the WFIRST-CGI Imager and IFS bands.

3. WFIRST SPACE ENVIRONMENT

As part of the current design cycle (cycle 6), the WFIRST project is carrying out a trade between a geosynchronous orbit and an L2 orbit similar to that of the James Webb Space Telescope (JWST). If the project selects the L2 orbit, then it is most likely to be a direct insertion orbit whose trajectory through the Earth's trapped-particle radiation belts will be very short and inconsequential. Therefore, the exposure to harmful radiation in general is lower at L2 compared to geosynchronous orbit.

To calculate the radiation environment for the WFIRST-CGI detector in L2, we ran the radiation transport computer code for a geosynchronous orbit and subsequently removed the contribution from the Earth-trapped protons and electrons, leaving only the solar proton fluence, common to both geosynchronous and L2 orbits. To verify this approach, a comparison was made between the JPL model prediction of the L2 environment for
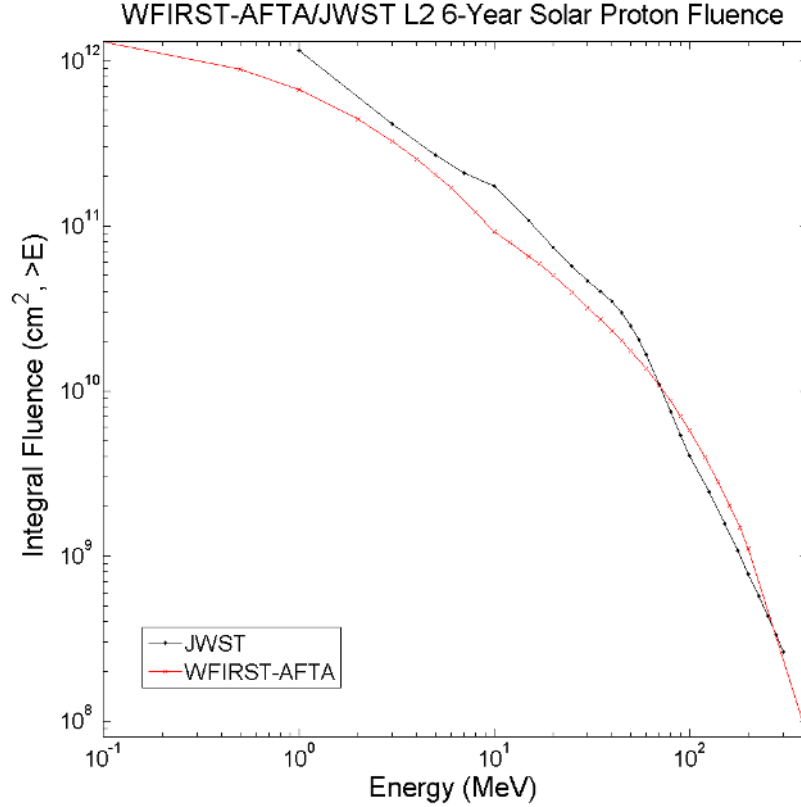
Figure 4. Comparison of independent predictions for the solar proton fluence in a direct insertion L2 orbit for the WFIRST and JWST missions. WFIRST data were calculated based on the JPL 91 Solar Proton model at a 95% confidence level and with a radiation design factor (RDF) = 2. JWST data were scaled to 6 years based on 5-year data taken from "The Radiation Environment for the JWST" (JWSTRPT- 000453).[35]

WFIRST and the Goddard Space Flight Center (GSFC) model prediction of the L2 environment for the JWST mission. Since different NASA centers use different validated radiation models, the comparison serves as an independent corroboration. The graph in Fig. 4 shows the solar proton fluence as a function of particle energy for WFIRST and JWST. The WFIRST model prediction is only slightly lower than that of JWST. The WFIRST data were calculated based on the JPL 91 Solar Proton model at a 95% confidence level and with a radiation design factor (RDF) of 2. JWST data were scaled to 6 years based on 5-year data taken from "The Radiation Environment for the JWST" (JWST-RPT-000453).[35] Based on this comparison, it was concluded that our methodology was sound.

A radiation transport model, NOVICE (Jordan et al. 2006[36]), was used to calculate DDD and total ionizing dose (TID) in the IFS EMCCD die. A three-dimensional (3-D) mass model of the EMCCD package and radiation shield computer-aided design (CAD) (shown in Fig. 5) was used for the radiation transport calculation. Shielding is essential to limiting radiation-induced damage. To assess the DDD and TID in the CCD die, seven "dose detectors" along the CCD die center perpendicular line were selected. Thus, the dose levels were calculated at the detector surface and bulk depths of 2.54, 10.16, 25.4, 101.6, 254, 508, and 640 μm.

The radiation transport model revealed that there is a significant difference between geosynchronous and L2 orbits for the damage due to TID, whereas there is negligible difference between the two orbits for the damage due to DDD. Using the radiation model, it was determined that a 1-mm-thick glass window in front of the EMCCD reduced the TID level in the surface layer to only 1 krad (RDF = 2) for a radiation shield of 10-mm thick tantalum. The radiation transport calculation incorporated a 3-D CAD mechanical model of the camera package enclosed by a cylindrical radiation shield, as shown in Fig. 5.
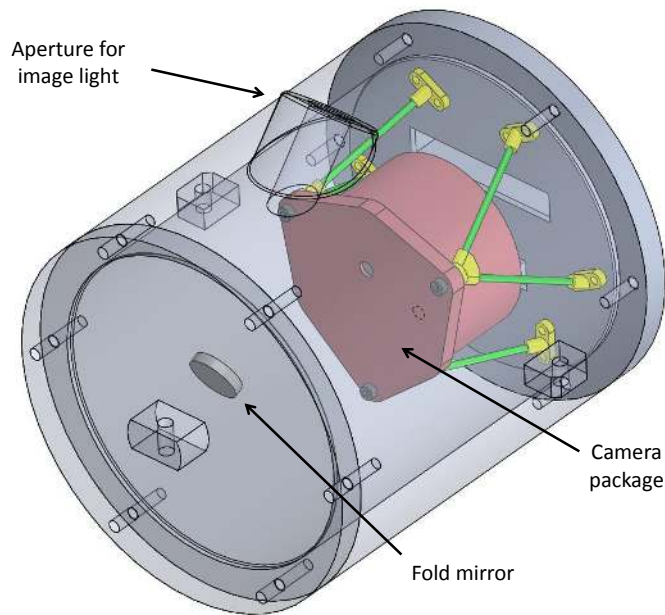
Figure 5. Computer-aided design (CAD) model for the detector package and radiation shielding, shown 10-mm thick. The shielding was designed for radiation analysis. The camera package is mounted inside a cylindrical drum radiation shield as shown. The radiation simulation compared different thicknesses of both tantalum and aluminum shielding material.

Figure 6 shows the expected radiation exposure of the WFIRST-CGI detectors over the span of a 6-year mission in geosynchronous and L2 orbits, for both DDD and TID, respectively, for a range of tantalum and aluminum shielding thicknesses and including a 1-mm-thick glass window placed in front of the detector. The model used the required RDF of 2. The design for the EMCCD shielding material and thickness will later be refined based on the results of the phase II radiation testing to be conducted in the summer of 2015. The DDD radiation doses to be used in phase II will span the radiation levels across the family of curves shown in Fig. 6. In phase II, we will measure the detector performance degradation as a function of DDD fluence. Then, the shielding material and thickness will be chosen to correspond to an acceptable EOL performance degradation.

Based on the above radiation analysis, it was concluded that so long as a 1-mm-thick glass window is used in front of the detector, TID will be reduced to very low levels and DDD is the primary risk to EOL detector performance.

4. RADIATION DAMAGE

4.1 EMCCDs for the WFIRST-CGI

CCDs have been extensively developed and applied for precision measurements in space, beginning with NASA's Galileo spacecraft and the HST, and continuing to the present with large focal planes on Kepler, Gaia, and Euclid. Radiation environments in space and their effects on detectors have been extensively studied, and NASA/JPL have developed tools for modeling and testing the effects of such environment on CCDs.[22] Despite the extensive heritage of silicon detectors in space, there is at present no flight-proven detector technology that meets WFIRST-CGI requirements.

As outlined in Sec. 1.2, the JPL detector trade study relative to the WFIRST-CGI stringent requirements for sensitivity and S/N identified that the CCD201 proved to be the most promising detector in meeting such performance. However, for the purpose of comparison, this study assumed BOL performance only where degraded sensor performance, a consequence of radiation damage in the form of TID and DDD, was unknown, since EMCCDs had not yet been empirically tested for such degradation.
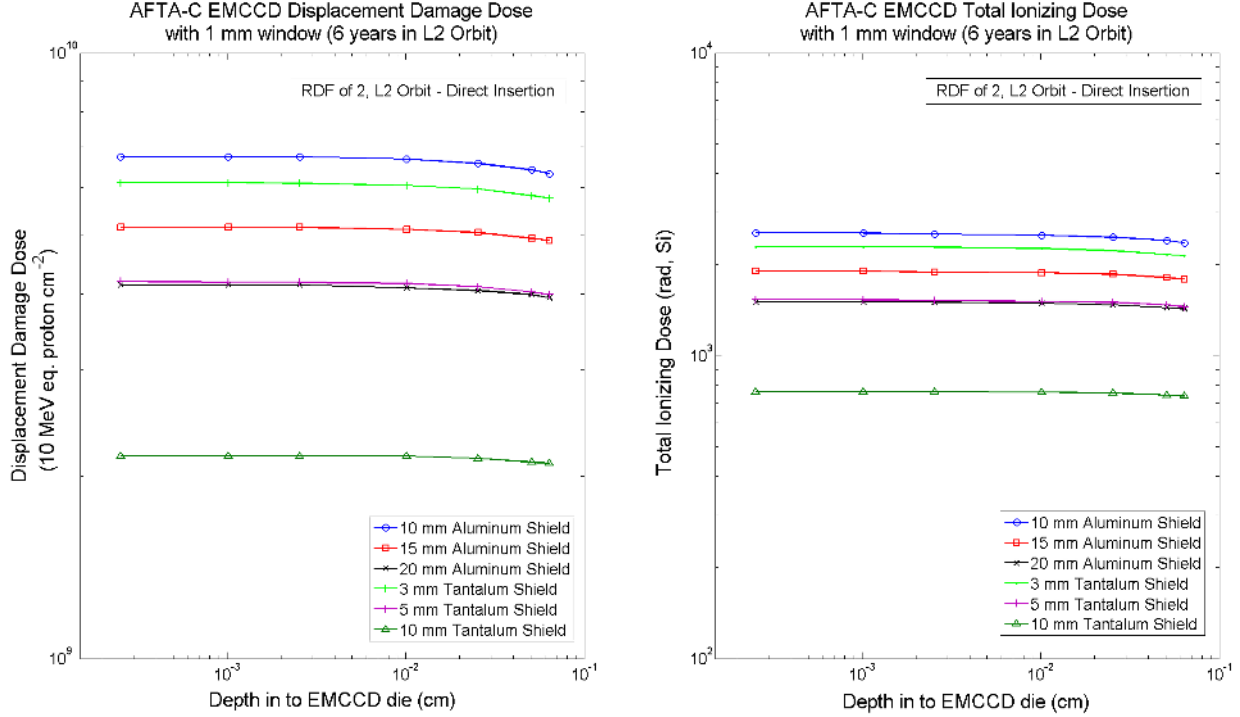
Figure 6. *(Left)* Logarithmic plots of DDD (10 MeV equivalent protons cm^{-2}) as a function of depth in the EMCCD (cm) with a 1-mm-thick glass window. This is for an L2 orbit (direct insertion) for an RDF = 2. DDD is shown for a range of various shielding materials and thicknesses. *(Right)* Logarithmic plots of TID (rad, Si) as a function of depth in the EMCCD (cm) with a 1-mm-thick glass window. This is for an L2 orbit (direct insertion) for an RDF = 2. TID is shown for a range of various shielding materials and thicknesses.

In this context and in order to advance the TRL of EMCCDs, it is therefore critical to understand the risks of radiation damage and their mitigations. Although there are some previous studies of radiation effects on CCD201 detectors,[17] these studies are not sufficient to demonstrate the EOL performance in the WFIRST environment or its projected measurement conditions. Consequently, the WFIRST-CGI requires experimental verification of EOL performance of CCD201 detectors in a realistic radiation environment.

4.2 Radiation Damage Effects on Detectors

In normal operation, light entering a CCD will interact with the silicon to produce electron-hole pairs. CCDs form images by first collecting photogenerated charge over a period of time (charge storage) and then measuring the accumulated charge as a function of location on the detector (readout). Latent images comprise accumulated charge stored in capacitors within the array, and images are "read" by serially transferring collected charge through the coupled capacitors in the array toward an output amplifier that converts charge packets to an analog voltage output signal. EMCCDs further incorporate a high-gain register, which uses high electric fields to amplify the charge. Maintaining CCD performance within specifications depends on charge trapping and detrapping properties of silicon, oxides, and silicon-oxide interfaces, all of which are subject to degradation due to radiation exposure.

Silicon detectors exposed to high-energy photons, electrons, and particles suffer damage to both the silicon and the oxides that together comprise the capacitors making up the CCD structure. Particles and photons incident on the array transfer energy to the CCD along their paths, leaving behind damage in the form of broken chemical bonds and charged defects. Occasional interactions with nuclei can further damage the detector by displacing silicon atoms from their ordered locations within the crystal lattice. These two types of damage–ionization and displacement damage–create defects and traps that affect the detector performance in distinct ways.
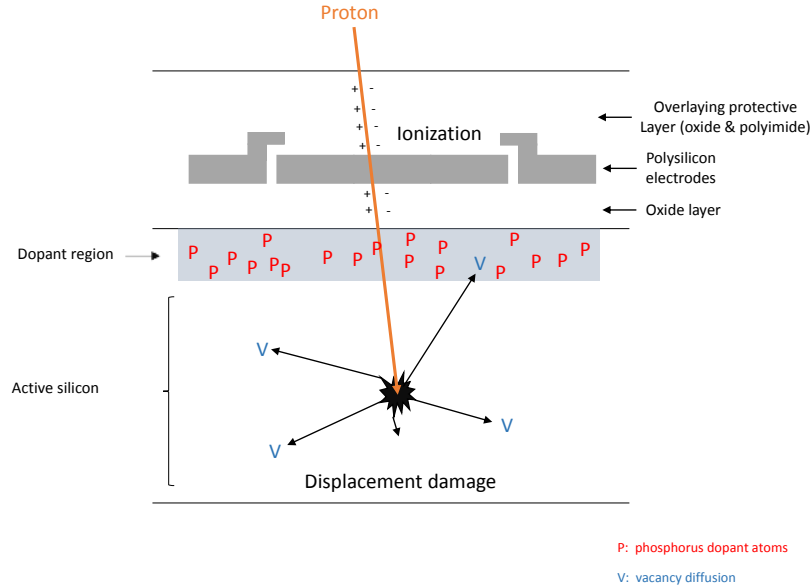
16

Figure 7. Illustration of radiation damage mechanism for a high energy proton in an EMCCD, much like the damage that the CCD201s have undergone in this study. Adapted from Hall et al.[38]

4.2.1 Total ionizing dose

Charged particles, x- and gamma radiation in the space environment damage oxides and surfaces, leaving a trail of broken chemical bonds in silicon oxides and interfaces. The resulting defects act as electron and hole traps, leading to time-variable charging of the oxide and the silicon-oxide interface, which, in turn, affects the internal electric fields in the silicon detector. The resulting "flat-band voltage shifts" alter the operation of CCDs by changing the internal electric fields that direct and guide signal electrons in their path to the output amplifier. Shifting bias voltages can degrade detector performance by altering FWC, CTI, and CIC. In an EMCCD, radiation-induced flat-band voltage shifts can degrade multiplication gain. Radiation-induced traps formed near the thinned, illuminated surface of the CCD201 are subject to variable (time-dependent) charging, resulting in decreased QE, instabilities and image artifacts, including persistence and QE hysteresis. Interface traps are also responsible for increased surface dark current and loss of signal due to surface recombination. Moreover, the oxide and interface traps that are responsible for these effects can change with time, which introduces time and temperature dependencies and performance instabilities in radiation-damaged devices.

The severity of the radiation-induced degradation depends on the oxide thickness and composition, as well as the processing parameters used to form the oxide. e2v has developed radiation-hardened oxides to mitigate these effects, reducing the flat-band voltage shift from the typical values of 100 to 200 mV/krad (Si) in standard devices to 6 mV/krad (Si) in devices fabricated using radiation-hardened oxides.[37] However, EMCCDs have not been fabricated using a radiation-hardened oxide and there would be some technology development and associated risk required to do so. A radiation-hardened oxide is complicated by the unusual conditions required to operate the multiplication register. We suggest that the most effective design modification for improvement of radiation hardness would be a reduction in the charge channel width, which would reduce the cross section for radiation-induced traps.

4.2.2 Displacement damage

Displacement damage and trapping. Energetic particles such as protons and neutrons can damage detectors by displacing silicon atoms from their lattice sites in the silicon crystal (see Fig. 7). Silicon vacancies are associated with energy levels in the silicon bandgap, which can capture photogenerated electrons and holes. One effect of

Table 6. Most common types of traps and physical trap parameters in silicon.[38] These reflect a sensor temperature of –114° C. We refer the reader to Hall et al.[38] for a discussion on trap cross section and emission time. These must be considered when minimizing CTI based on the dwell time of a charge packet under an electrode.

Trap	Defect	Average energy relative to conduction band (eV)
Si-A	Oxygen-vacancy complex	0.17
(V-V)- -	Divacancy, doubly ionized	0.21
Unknown	Unknown	0.30
(V-V)-	Divacancy, singly ionized	0.41
Si-E	Phosphorus-vacancy complex	0.46

traps is therefore a degradation of detector sensitivity and increased noise, as trap-assisted generation and recombination events cause a loss of signal and increase the bulk dark current. The greatest impact of displacement damage on detector performance comes from the smearing of charge that results from trapping and subsequent detrapping of electrons, leading to artifacts, such as image persistence and deferred charge.

Trap species and characterization. Isolated vacancies in silicon are unstable, and vacancies will migrate through the crystal until they interact with other defects to form a stable configuration. The most common trap species in radiation-damaged silicon are divacancies, phosphorus-vacancy complex, and oxygen- vacancy complex. Each of these forms a distinct set of trap states in the silicon. Table 6 shows these common radiation-induced defects and traps with their associated energy levels.

Once the trap properties are known, the dynamics of electron trapping and detrapping events can be modeled using Shockley-Read-Hall theory.[39] The degradation of CCD performance depends not only on the density, location, and type of traps present in the detector but also on CCD operating parameters, such as detector temperature, bias voltages, and clock frequencies. If these parameters can be measured and/or calibrated, it becomes possible to correct for trap-induced errors using image postprocessing algorithms. Deferred charge can be corrected on the HST to a precision of 97%, and work is ongoing to improve correction algorithms to achieve 99% accuracy for the ESA Euclid mission. However, image correction algorithms run into limitations at low signal levels. For example, even with perfect knowledge of the trap locations and properties, capture and emission times for trapping/detrapping events are stochastic, so that the accuracy that can be achieved by image correction algorithms depends on the number of photons detected.[23, 25, 30, 40]

4.3 Associated Risks

4.3.1 Radiation-induced degradation of detector noise

The CCD201 noise floor must be sufficiently low over the lifetime of the mission that the WFIRST-CGI can detect the faint signals from planets orbiting distant stars. Because detector noise degrades over time due to radiation exposure, meeting this requirement will entail measuring several key detector parameters as functions of radiation exposure. Among these key parameters are dark current, CIC, multiplication gain, and read noise. In order for these results to be applicable for the CGI, CCD201 noise performance must be characterized using operating parameters that are relevant to a realistic environment for the mission, including any background signals that may affect low-light level sensitivity. In particular, the CR background is a threat to low-light level detection on the CGI because of the potential for CRs to contribute to the noise floor. While it is possible to subtract CRs from images during image postprocessing, residual noise from this subtraction (such as shot noise) could dominate the detector noise in the affected pixels. As a result, the CGI detector frame rate must be kept short enough to prevent the CR background from dominating the noise floor. It is expected that the CGI will be required to collect and coadd multiple frames during the instrument integration time, using postprocessing to remove CRs from individual image frames. In addition, the large-signal events generated by CRs, coupled with the finite well capacity of the high-gain register, are expected to impose a constraint on the maximum usable

gain setting. Finally, the EMCCD gain degrades over time (through a process commonly known as "aging"), and this degradation must be characterized under realistic conditions because the EMCCD gain directly affects the EMCCD noise floor.

4.3.2 Cosmic ray & other particle rates (ground-based)

We conducted a study at JPL to estimate the number of CR events at ground level that an EMCCD under high-gain conditions would be sensitive to. This study was carried out in order to investigate the optimum WFIRST-CGI integration times based on these particle densities with the view to ultimately investigate their effect on the device CTI. We found that when using conventional CR identification and removal algorithms, the CR core (which we define as the area where the main strike occurred) was easily identified; however, we observed that in the event that such a particle had sufficient energy to saturate the high-gain register (after EM amplification), the algorithms were unable to fully identify pixel regions that were affected by this charge. This charge appears as a streak, or "tail", in the direction of charge transfer. In this study, we sought to identify the particle rate and the fraction of pixels affected by considering CR cores as well as CRs and tails. The algorithms presented in this work were designed to identify these regions only; they do not perform any postprocessing techniques to mitigate these effects on CTI. This will be considered at a later time.

We calculate a rate of 0.148 particles cm^{-2} sec^{-1} for the CCD201 (13-μm pixel pitch) and show these data in Figure 8. We found this by selecting appropriate acquisition settings that reflect the CGI conditions in order to meet dark current, CIC, and effective read noise requirements (EM gain of 450 was used), and exposed the sensor for integration times of 0 to 500 s, yielding as many as ~125 events for a 500-s exposure where the sensor was set up such that its orientation was parallel to the ground with no shielding. Each data point was calculated from 10 frames where the average number of events was calculated in addition to the fraction of pixels that were affected by both an event and/or an event and a streaked signal, or tail. Here, we refer to an event as a CR, or other particles that the EMCCD was sensitive to at these gain levels.

In order to identify and/or remove particles in the EMCCD that could increase device CTI, we developed an in-house detection and removal algorithm using the Python language from the Python Software Foundation.[45] We show a flowchart of this procedure in Fig. 9. The identification algorithm has three different classes: "Image Handler", "Section Group", and "Section". The "Image Handler" class first calculates the average pixel value in an image, identifies pixels above some user-defined threshold (this variable changes the aggressiveness of the algorithm), and assigns a flag to these pixels. Once these pixels have been flagged, they are broken up and distributed into Sections by the Section Group class. Here, we define a section as an array of pixel coordinates corresponding to flagged pixels as well as all adjacent pixels, e.g., those identified by the Image Handler. Each section is then sorted based upon two variables: (1) the size of a section in units of pixels and (2) the elongation of an event (e.g., a nonsymmetric core or a core and its tail). Each variable can change the aggressiveness of the algorithm and is user defined. The first variable checks how many pixels are in a section and the second variable defines the minimum required dimension ratio (length:width) in order for a section to be flagged as an event and a tail. Therefore, a section needs to be at least N times larger in one dimension than all of the other dimensions. These dimensions reflect a square or rectangular box, with eight reference points (N, S, E, W, NE, NW, SE, and SW). By establishing these points, the algorithm identifies the shape of a section. We found that a minimum length to width ratio of 1.5 was sufficient to identify nonsymmetric cores or cores and tails. The algorithm then takes sections that have passed both of the requirements and flags them as an event or events with tails. Finally, all flagged pixels are replaced with a value of –300 in order to easily neglect during image processing. This is also useful for estimating dark current rates for longer exposure times since false-positives are rejected. Finally, a pixel map is created where real pixels have a value of zero and events have a value of –300.

We note that each event profile on the detector has unique properties based on, e.g., the angle of the particle strike with respect to the detector surface, the length of the ionization trail, the device epitaxial thickness, the energy of the particle, the integration time, the employed EM gain and thus the degree of saturation in the high-gain register, etc. The depth of solar minimum and other synodic factors must also be considered for particle rates. Therefore, large frame-to-frame variation can be observed. In one frame, for example, there may be a large number of events that are tightly confined to smaller pixel areas where saturation in the high-gain register only occurs for a few pixels (number of events–higher; fraction of pixels affected–lower). A different frame may
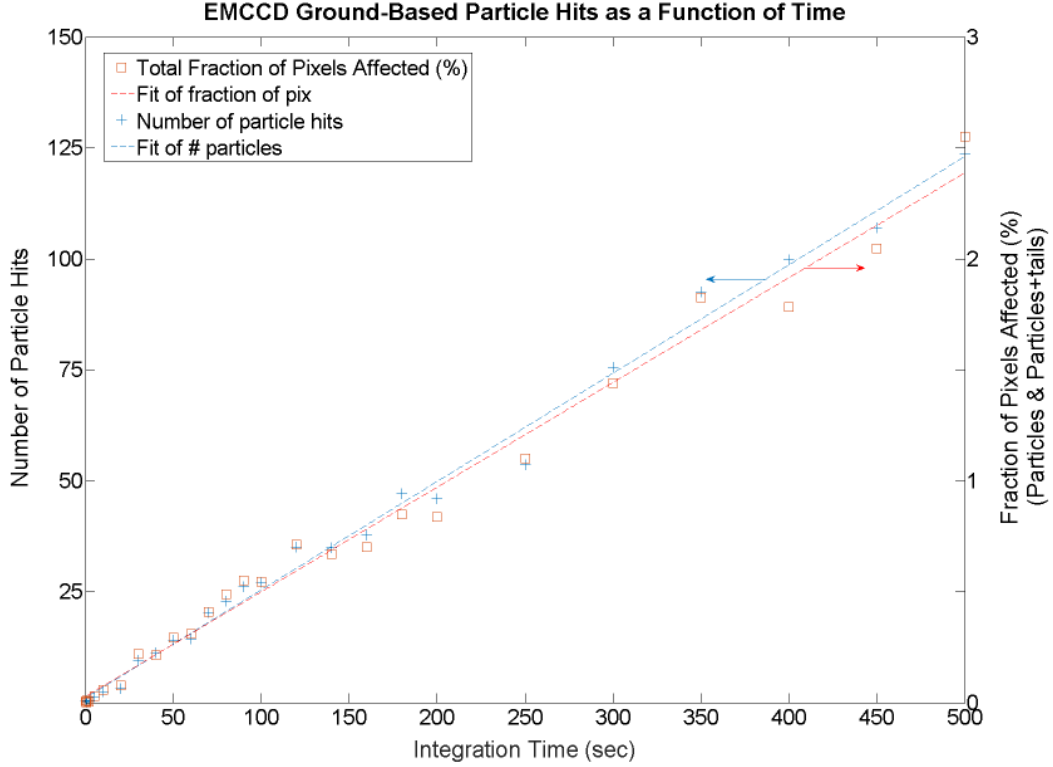
Figure 8. Plot of the number of particle hits (y-axis, a) as a function of integration time (s), and the total fraction of pixels affected (%, y-axis, left) as a function of integration time (s). The horizontal arrows point to which *y-axis* is relevant for each set of data. For this test, we selected acquisition settings that meet the WFIRST-CGI requirements, running at a temperature at $85°$ C and using an EM gain of 450. The total fraction of pixels reflects the full image area of 1024×1024 pixels.

contain less particle hits per unit area but with greater energy that are spread over many pixels as a result of saturation in the high-gain register (number of events–lower; fraction of pixels affected–higher). We note that this model does not take multiple particle strikes on one single pixel into account.

Other missions with L2 insertions, such as the Herschel Space Observatory, found record rates of CRs and other particles at launch, which they attributed to the depth of solar minimum at the beginning of the mission. These data were taken with Herschel's Standard Radiation Environment Monitor (SREM) where typical SREM count rates in L2 were $\sim 3 - 5$ particles cm^{-2} sec^{-1}; this range represents particles over a range of energies from $E > 0.5$ MeV – $E > 39$ MeV. We refer the reader to the SREM database[46] for data on the CR flux over the full mission, showing a higher concentration of CR flux at the beginning due to the solar minimum as indicated previously. These particle rates, coupled with the predicted solar cycle for the WFIRST launch, in addition to the range of particle energy levels in L2, must be considered for the CGI detectors. The ground-based study presented in this section indicates a small fraction of the expected particle rate in space. Our measured CR rate is higher than what is typically measured on the ground (~ 0.025 particles cm^{-2} sec^{-1});[22] however, ground-based particle fluence can vary greatly with altitude, in addition to other factors such as the presence of high-potassium BK7 glass causing secondary effects, whether a sensor is back-thinned as well as how thick it is or sensitivity to particles of different energies than other studies by using high EM gain. Device orientation can also affect the rate. We do not calculate energy levels or particle type in this paper but sought to identify any event that could potentially increase CTI. CRs are therefore included in this sample. In this respect, our study is being used to estimate optimum single-frame integration times to minimize CTI, currently estimated to be $\sim 100 - 300$ s. These frame times may be reduced further based on higher particle rates in orbit and the associated behavior of

Image Handler

a. Open file

b. Set any pixel *N* times > average pixel value to an arbitrary value

c. Assign flags

d. Threshold assigned; Data split up and passed to **Sections**

All pixels now identified as a CR or CR + tail are assigned value of -300

Section Group

Image split in to pixel sections

Req. 1 Determine the size of the Section

Req. 2 Determine shape of Section via 8 reference points (symmetric CR or elongated CR)

If *Req. 1* and *Req. 2* are passed, pixels flagged as CRs or CRs and tails

Sections

Cycle through image pixel values

Run check to confirm all values from **Image Handler (b.)** are present

If not: create a new Section

Add adjacent pixels to those in existing Sections lists

Cosmic Rays Removed

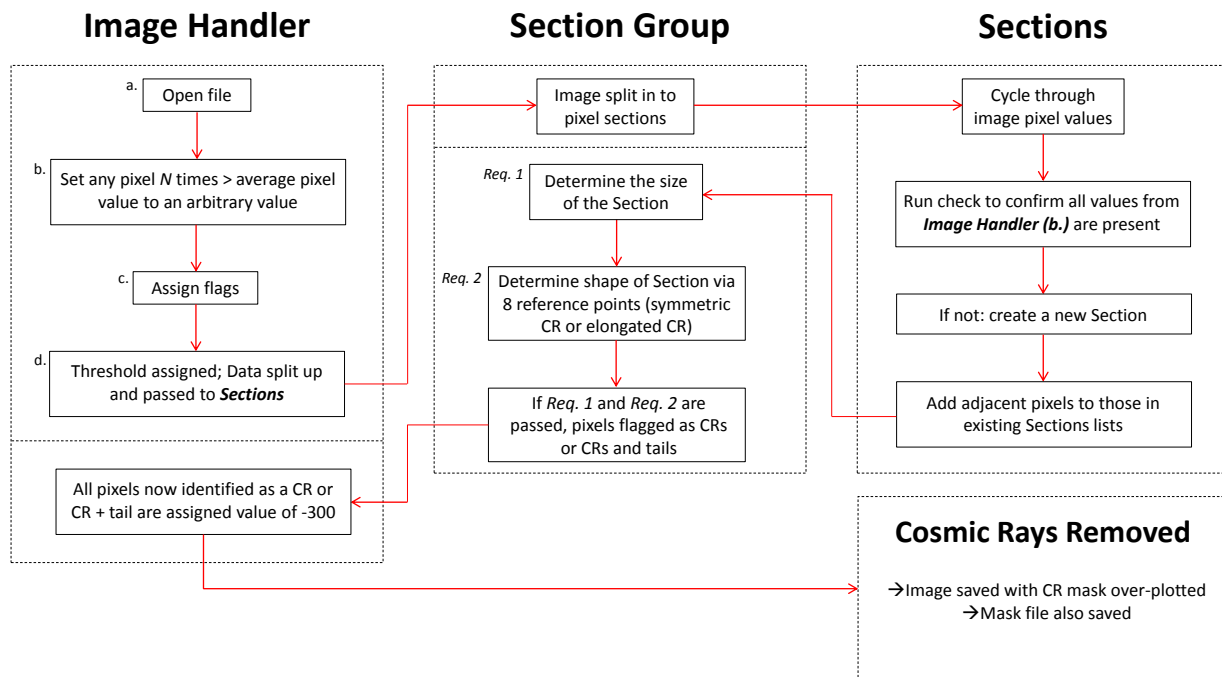→Image saved with CR mask over-plotted
→Mask file also saved

Figure 9. Flowchart of the custom EMCCD cosmic ray/other removal algorithm that was developed at JPL for this work. The three classes, *Image Handler*, *Section Group* and *Sections*, define the structure of the algorithm.

CTI. We intend to further extend this work to investigate such particle populations and how the acquisition time should be tailored to minimize CTI. Development of postprocessing techniques for the WFIRST-CGI detector application, such as those carried out on HST's WFC3 detectors must also be considered.[30]

4.3.3 Radiation-induced degradation of detector signal

The CCD201 must be capable of detecting faint objects even when the flux is low enough that it is necessary to detect single- electron signals in any given frame. Here, it is understood that it will be necessary to coadd many individual frames in order to achieve the required S/N. The major challenge is the effect of radiation-induced traps on CCD readout. While trap densities in "as-manufactured" detectors are exceptionally low, radiation exposure will cause significant accumulation of traps during the lifetime of the WFIRST mission. As described in Sec. 3, a radiation shield can extend the lifetime of the CCD201, but no amount of shielding can eliminate this accumulation of traps over time. Single-electron signals are vulnerable to a loss of spatial information as electrons can be trapped during readout and later released. In the limit of detecting single electron signals, it is an extreme challenge to obtain enough information to accurately correct images for trapping/detrapping events.

Recently, however, we point out that ESA, together with the Center for Electronic Imaging (CEI), have carried out a Gaia Radial Velocity Spectrograph (RVS) study, where test spectra were propagated through the RVS CCD sensors, including irradiated sections of the chips. They confirmed that a signal of 1.5 e$^-$ pix^{-1} could survive, and subsequently verified that subelectron detections were possible. This work is therefore extremely applicable to the WFIRST-CGI, and will be considered in the upcoming work with irradiated EMCCDs. Details of projected radiation damage to these sensors can be found in Seabroke et al.,[49] and the study confirming subelectron detections for CCDs that have been subjected to a high radiation dose can be found in Dryer and Hall.[41]

4.4 Single Event Gate Rupture in EMCCDs

A single event gate rupture, or SEGR, is when a heavy ion strikes a gate electrode of a MOS-type semiconductor device, such as an EMCCD, which subsequently damages the region where the gate lies. For a SEGR event,

the magnitude of this damage can depend on factors such as the ionization energy of the particle or the design of the device. Crucially, the voltages that operate in this local region where the incident ion strikes are also a major factor. Since an EMCCD's high-gain register can produce much larger local electric fields (3 MV cm^{-2} interpoly field) based on voltages approximately four to five times higher than a conventional register, this effect is of special relevance to an EMCCD device. See Sexton et al.[42] and references therein, for more discussion on the SEGR mechanism.

A previous study of the effects of SEGR has been carried out with an EMCCD sensor,[43] who used the CYClotron of LOuvain la NEuve (CYCLONE) at the Heavy Ion Facility (HIF), to investigate the resilience of EMCCD technology to the effects described above. Heavy ions in the space environment pose a risk of catastrophic failure in EMCCDs, because of the potential for an SEGR event to create a conductive path through one of the gate oxides in the gain register. In order to test this experimentally, an e2v CCD97 was used, which is a smaller format device compared to the CCD201, with an active image area of 512×512 pix and a 16-μm pitch. Simulations carried out prior to this test indicated potential gate rupture at $20 - 40$ MeV cm^{-2} mg^{-1} and therefore linear energy transfers (LETs) of 58.8 MeV cm^{-2} mg^{-1} were used (the highest LET available at the HIF), with 16-μm penetrating depth. Different flux levels and amplification gain settings were used; however, the CCD97 did not undergo a catastrophic failure due to gate rupture. The multiplication gain was then increased and the angle of the HIF changed to produce an apparent LET of 135 MeV cm^{-2} mg^{-1} in an attempt to induce a gate rupture. Again, the device survived the test.

This test was successful in demonstrating that there was no sign of a SEGR event for an EMCCD under high-gain conditions. Furthermore, a spacecraft in L2 orbit is subjected to $\sim 10^6$ heavy ions m^{-2} over 5 years with an LET of 60 MeV cm^{-2} mg^{-1}, and the fluxes tested in the Evagora et al.[43] study were sufficiently high to conclude that the probability of an ion incident on a sensitive region of the device in orbit would be small. We note that SEGR events are still possible in EMCCDs; however, this result suggests that even by considering the higher local electric field conditions present in an EMCCD under high gain, such a device should not be affected by heavy ions in orbit over the WFIRST projected lifetime. Finally, another study by Smith et al.,[44] who subjected 100 CCD97 EMCCDs to a proton fluence of 2.5×10^9 protons cm^{-2} (10 MeV equivalent), also reported no device failures, where they were specifically concerned about irradiation of the high-gain register to investigate any kind of unexpected catastrophic failures.

5. EMCCD BEGINNING OF LIFE PERFORMANCE

5.1 EMCCD Camera and Test Conditions

BOL performance of a "science-grade" CCD201, e2v's highest standard in terms of minimal defects and maximum performance, was carried out, where the three main criteria assessed were read noise, dark current, and CIC. We discuss CTI in Sec. 6. The Nüvü Cameras EMN2 camera with the CCCP controller[47] was used to perform this characterization work. The EMN2 is a liquid nitrogen (LN2) cooled system, allowing deep sensor cooling as low as -105 $\pm$ 0.01° C (168.15 K) under calibrated gain. Crucially, the sensor is driven by the "CCD controller for counting photons", or CCCP, which facilitates full control over all clocking architecture, allowing waveform design and modification. The motivation to procure this camera was therefore a direct result of this functionality, enabling JPL to commence an early investigation into the desired clocking design for optimal CGI operating conditions.

BOL testing of the CCD201 was carried out over a range of temperatures using both the conventional and EM outputs as well as all combinations of vertical clocking frequencies and horizontal read out rates. A self-pressurized 160-l LN2 dewar, vacuum-jacketed transfer line and bayonet were used to maintain the desired temperatures throughout the testing. The device was run in IMO for maximum dark current performance, and the serial register was run in its standard NIMO in order to minimize CIC since EM-generated CIC will dominate in the high-gain register. The serial register is also flushed in order to clean residual charge that may have been accumulated. This process will generate CIC in the leading N pixels; however, typically read noise will dominate at these levels. For this application under high multiplication gain, we sought to fully suppress any CIC component and therefore the next clocking sequence ignores the first N pixels prior to read out. Initial device bias conditions as outlined in the CCD201 specifications sheet[48] were used. These were modified thereafter to produce

Table 7. Measurements of native readout noise (unity gain) of the CCD201 EMCCD using the NüVü EMN2 camera and CCCP controller. We note that column 5 denotes what gain factor is required based on the read noise calculation in column 3 in order to meet the WFIRST-CGI effective read noise requirement of 0.2 e$^-$ rms. $k-$gain is the conversion gain.

Amplifier	Horiz. Frequency (MHz)	Read Noise (e$^-$)	$k-$gain (e$^-$ DN^{-1})	Gain Factor [$\sim$0.2 e$^-$ rms]
Conventional	0.1	3.84	3.30	...
Conventional	1	9.24	3.27	...
Conventional	3.33	12.57	3.31	...
High gain (EM)	1	33.66	15.30	$\sim$75
High gain (EM)	5	75.96	18.99	$\sim$90
High gain (EM)	10	89.78	17.82	$\sim$450
High gain (EM)	20	253.42	24.13	$\sim$1220

the highest S/N performance by reducing the read noise and minimizing CTI within the multiplication register. The high voltage clock (Rϕ2HV) voltage was adjusted where necessary in order to change the multiplication gain applied. We used multiplication gains of up to $\times$1000 for dark current measurements with the EM register and for all CIC measurements. This reduced the effective readout noise to sufficiently low levels so that CIC and other spurious noise could be detected and assessed. It also allowed for much shorter integration times for dark current frames. All dark current data were taken under zero illumination conditions

5.2 Read Noise and Conversion Gain

The read noise (e$^-$ pix^{-1}) of a detector is generated during the readout process, where there is noise associated with the conversion of charge to an electric impulse as charge packets are moved through a MOSFET transistor. This noise is limited by on-chip amplifier noise but can also be attributed to other sources of noise that are independent of the incoming signal. Amplifier noise has many components, including Johnson, Reset, White, Flicker (1/f), Shot, Contact and Popcorn (see Janesick[22] for more information). During the output process, photoelectrons are converted to an analog signal and subsequently into a digital number (DN). This conversion is described by the conversion gain factor, measured in e$^-$ DN^{-1}.

The native read noise (where no EM gain was applied) and conversion gain (hereafter k-gain) for the CCD201 were measured from a photon transfer curve by using standard techniques,[50] for each output amplifier, at different vertical frequencies and horizontal readout rates. All data used for this measurement were bias subtracted, which removes any gradients or fixed pattern noise since these cumulative effects will increase any computed standard deviation in raw images. This is important when assessing any overscan regions, which we used as additional confirmation of the native read noise. We show the measured values of read noise and conversion gain in Table 7, where column 5 denotes the gain factor that is required, based on the native read noise calculations from the CCD201, in order to achieve effective read noise performance of $\sim$0.2$^-$ rms, as currently stipulated by the WFIRST-CGI detector requirements.

5.3 Dark Current

Dark current is caused by thermal generation of minority carriers and is common to all semiconductor devices. Although running a device in IMO or NIMO can cause large differences in dark current, ultimately the only solution to suppressing dark current is achieved by cooling the device. The three main sites in a device that contribute the most to dark current are bulk regions below the potential well and channel stops, depleted material in the potential well, and Si–SO2 interface state contribution from the front- and backside of thinned CCDs, like the CCD201. See Janesick[22] for more details. Because we run the CCD201 in IMO, the surface dark current component is greatly reduced, and dark current is dominated by generation in bulk silicon. We sought to measure dark current over a range of temperatures in order to identify a threshold temperature that meets that CGI dark current requirement.
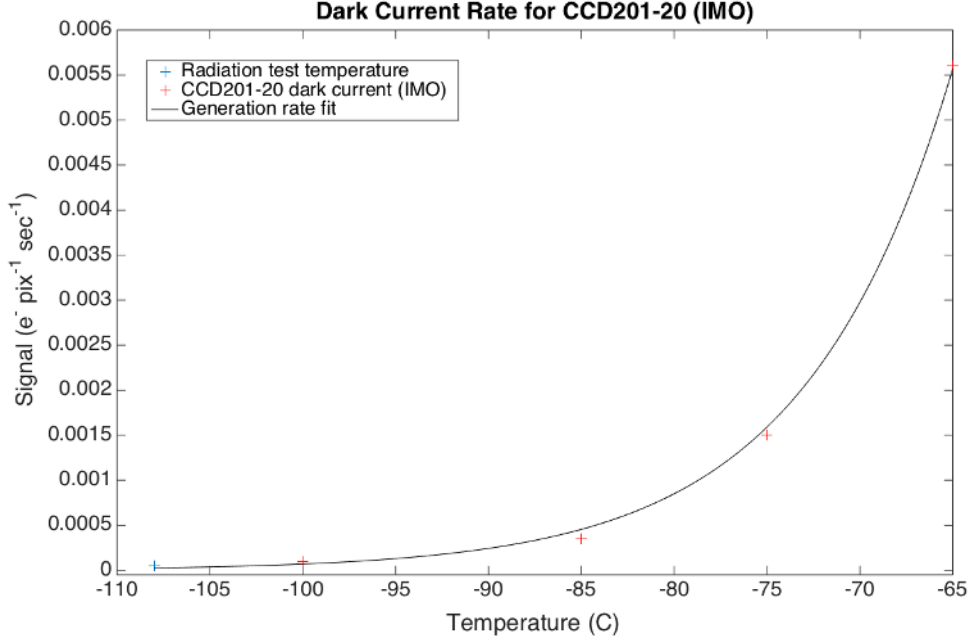
Figure 10. Plot of signal as a function of temperature as measured from the CCD201 using the EMN2. For this characterization, dark current was measured over temperatures from -105° C to -65° C. We used the EM amplifier with a gain of 1000 to sufficiently suppress the read noise. The calibrated gain range of the EMN2 only allows gain to be employed from -65° C to -105° C. We also include the dark current datapoint at -108° C, which was measured from one of the CCD201s prior to irradiation at the PSI facility, in Switzerland, which is shown in the bottom left corner as a blue cross.

Dark current data were taken over a range of -105° C to -65° C (168.15 K – 208.15 K) using the EM amplifier under a multiplication gain of 1000. Under such high amplification, the read noise contribution becomes negligible, which allows dark current to be measured over integration times of minutes. We obtained data for 13 different integration times from 0 to 300 s under zero illumination conditions. Before dark current assessment, these data were bias subtracted and all CR contributions were removed. CRs were removed as outlined in Sec. 4.3. We neglected the outer 100 pixels in both X and Y in order to avoid edge effects.

The WFIRST-CGI dark current requirement, which is based on the planetary models described in earlier sections, is 5×10^{-4} e$^-$ pix^{-1} sec^{-1}, which reflects a dark current at -85° C, see Fig. 10. Since the projected CGI observation time is currently of order 100–300 s, it is vital that dark current is minimized as much as possible. Maximum cooling is the first obvious solution such that thermal excitation is minimized; however, it has been shown that for temperatures less than -85° C, CTI can occur under high-gain conditions, possibly as a result of charge clouds interfacing with surface states. This might cause smearing of CRs or other charge packets with sufficient energy. Work is ongoing at JPL that is investigating the tradeoff between dark current and CTI performance for the WFIRST-CGI. However, the CCD201 passes the dark current requirement for all temperatures less than -85° C. This performance will degrade as a function of radiation exposure in orbit; we investigate these effects and provide a discussion in Sec. 6.

5.4 Total Spurious Contribution: Clock Induced Charge and Other

CIC is a source of spurious generation in CCDs that occurs on the rising edge of a clock when a phase comes out of inversion. Therefore, by running a CCD in IMO, surface dark current is greatly suppressed at the expense of higher CIC.[22] When a clock pushes the surface into inversion, holes from the channel stop migrate to the surface but some get trapped in the Si–SO2 interface; however, upon subsequent clocking of the surface out of inversion, holes are accelerated from the surface to the channel stops, potentially producing CIC by impact ionization. The negative-to-positive potential switch under the electrode supplies sufficient energy for this process to generate and collect charge in the potential well, also known as CIC. This generation is a function of the number of transfers,

24

Table 8. Measurements of total spurious generation (CIC and other) for the CCD201 EMCCD using the Nüvü EMN2 camera and CCCP controller. We note that V_{SS} is the substrate voltage. The CIC quoted here is the total signal from the image section and the high-gain register.

Amplifier	Horiz. Rate (MHz)	Vert. Freq. (MHz)	EM Gain	V_{SS} (V)	Total Signal (e^- pix^{-1} $frame^{-1}$)
High gain (EM)	1	1	1000	4.5004	1.05×10^{-2}
High gain (EM)	5	1	1000	4.5004	3.20×10^{-3}
High gain (EM)	10	1	1000	4.5004	1.25×10^{-3}
High gain (EM)	10	0.2	1000	4.5004	8.75×10^{-3}
High gain (EM)	20	1	1000	4.5004	2.20×10^{-3}

but at a lower level, the clock amplitude, the clock swing, and the resolution of the clock edges all contribute to greater CIC. Dark current and CIC are the most dominant source of detector noise in the WFIRST-CGI environment, and as a result, strict requirements have been placed on the detector in order to achieve $\leq 1.8 \times 10^{-3}$ e^- pix^{-1} $frame^{-1}$ of CIC. This requirement assumes some margin since modification of the sensor's clocking architecture may be required based on as yet unknown CTI, resulting in a trade-off between CIC and CTI. It can be difficult to disentangle CIC and dark current, in addition to other sources of noise in a detector. One way to assess CIC is to take data at zero integration timescales at low temperatures (e.g., -85° C), thereby minimizing the expected thermal excitation by an order of magnitude with respect to CIC per given transfer. Therefore, for this component of this work, we have designed a test that yields low enough dark current signal so that CIC and other spurious charge can be measured. Similarly, we employ EM gain to sufficiently suppress readout noise levels for all horizontal readout rates. We could not calculate CIC for the conventional amplifier, since any measurement is inherently read noise dominated.

Zero integration, zero illumination frames taken at -85° C, were obtained using the EM amplifier for each horizontal readout rate as well as different combinations of vertical clock frequencies, where a gain of 1000 was used in all cases. An output histogram of 20 frames per given acquisition mode combination was produced, and a Gaussian fit was applied to the read noise section of this plot, as shown in Fig. 11. We applied a 5.5σ threshold, indicated by the red dashed vertical line, to the mean of the Gaussian plot, which represents the mean of the read noise. This threshold was best representative of the point at which spurious signal was getting amplified by the high-gain register. We then integrated under the curve to the right of this threshold and calculated the total signal, per pixel, per image. Based on a temperature of -85° C, we removed any expected dark current contribution as measured in Sec. 5.3. The result was a measure of all spurious generation in the system for a given mode, including CIC and other. We show these measurements in Table 8. We note, however, that measuring CIC using this method can sometimes be misleading if a system's CTI in the serial direction has not been characterized well. We show the measured CIC signal decreasing with increasing serial clock speed where this rate is roughly inversely proportional to clock frequency. However, there is a small increase from 10 to 20 MHz that does not follow the trend. If CTI effects are present for the 20-MHz timing, charge packets might spill into a pixel that follows another, or beyond, and will increase the number of pixels that exceed the 5.5σ threshold outlined previously. We show another way of measuring CIC in Sec. 6.4.3.

Finally, we highlight that JPL is currently conducting an investigation as to why the total signal, as measured in these data, appears to be higher for lower readout rates, where alternate clocking techniques are being considered. Since the CIC mechanism is believed to be due to holes escaping from traps at the surface and producing electrons by impact ionization given sufficient energy, the longer there is a high potential difference between two phases, the higher the probability that a hole will escape and be subjected to a higher field. It may be this time dependence that results in faster clocks producing less CIC. Importantly, as noted previously, any decreasing serial CTI might contribute to apparent higher CIC levels; therefore, CTI measurements for all clocking implementations will also be measured. These considerations become important for flight electronics, since higher readout rates are inherently more difficult to accommodate for flight, based on requisite components that are highly temperature and radiation sensitive; these components are unique to a design that facilitates faster clocking. This work is ongoing.
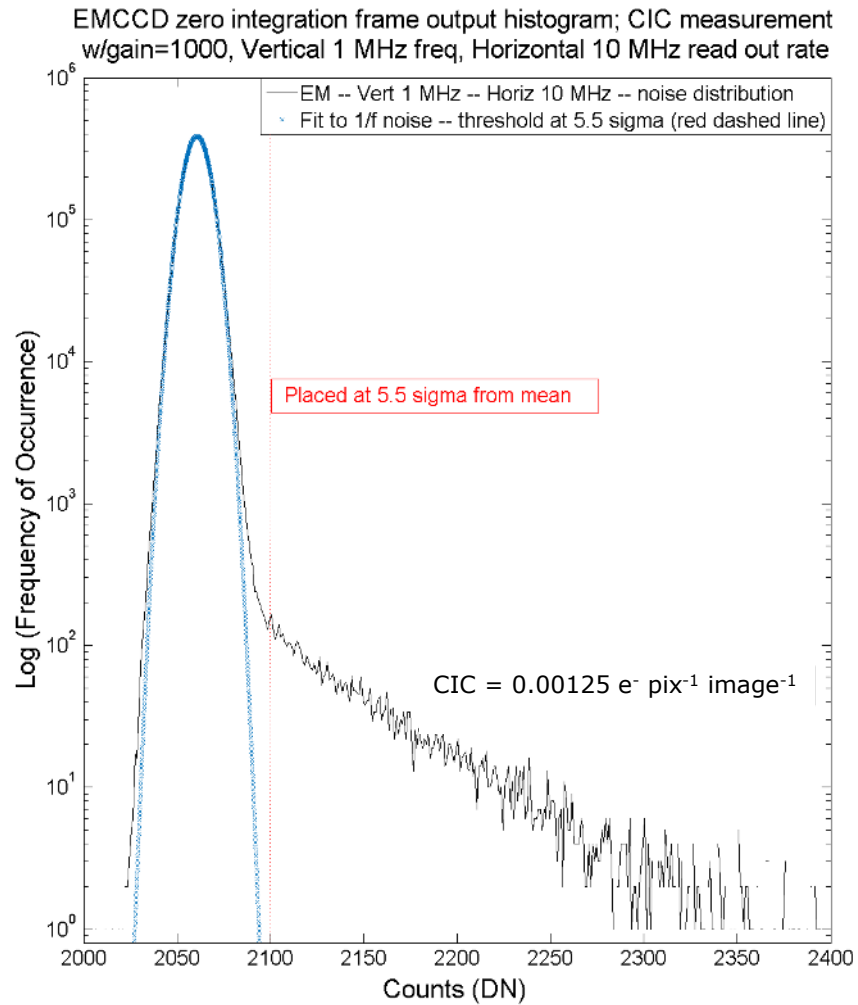
25

Figure 11. Histogram of 20 EMCCD frames, taken at a gain of 1000. The Gaussian function to the left is the read out noise (primarily 1/f) with small amounts of CIC and dark current. The data points to the right of the 5.5σ are the total contribution of CIC, dark current and other spuriously generated charge. The 5.5σ threshold was applied to the mean of the blue Gaussian fit to the read out noise. When calculating CIC, we integrate under this curve, and scale by the total number of pixels per given image, and remove the dark current for this temperature. The result is charge generated from CIC and other spurious sources.

26

5.5 Reducing the Noise Contribution

Since the total spurious noise in an EMCCD, which we define to be the contribution from dark current and CIC, can be amplified by the EM register, it is the dominant source of noise since readout noise is suppressed under such amplification. As discussed previously, thermal excitation resulting in dark current can be greatly reduced by deep sensor cooling in addition to running the device in IMO. However, since the CIC can vary strongly as a function of clock swing, clock rise time as well as the device bias conditions (in addition to waveshapes, as reported by Daigle et al.[31]), it is thus heavily dependent on the clocking process and how these parameters are designed in order to transfer charge.[22] Indeed, careful consideration of a device's clocking design also minimizes the CTI. Here, we show the different sources of noise inherent to an EMCCD, which must be considered in all performance modeling of such a device, and highlight these differences when compared to conventional devices. Additionally, we outline the different operating modes and the importance of precision clock timing in order to reduce CTI for the WFIRST-CGI application.

5.5.1 Noise in EMCCDs

Evaluating the S/N in an EMCCD is much like that of a conventional CCD; however, since there is a gain factor applied during the EMCCD amplification process, the equivalent readout noise, eff_{RN}, is reduced by an amount R/G, where R is number of electrons and G is the amplification gain. However, as previously outlined in Sec. 2, there is an added variance in the signal, the ENF, based on the stochastic nature of the process. Therefore, when calculating the S4N for an EMCCD, the read noise becomes negligible but the ENF and multiplication gain must be included, in addition to other standard parameters, such as the QE and the total signal in photoelectrons, S, where $S = P \cdot QE \cdot t$. The terms P and t are the incident photons and integration time, respectively. The principle sources of noise are found via the root of sum of squares law and the S/N equation is thusly calculated as shown (adapted from McLean et al.[51]):

$$S/N = \frac{S}{\sqrt{2S + (\frac{R}{G})^2}}, \tag{4}$$

where S becomes $2S$ in the denominator representing the noise, because of the ENF adds to the photon shot noise where the uncertainty now becomes $\sqrt{2S}$ as opposed to $\sqrt{S}$ (ENF= $1.41^2 \sim 2$). Most importantly, although the read noise gets reduced by R/G, the pixel charge handling capacity will also be reduced by this same factor. Although the CGI application will produce an expected photon flux in flight of order 2×10^{-2} photons pix^{-1} sec^{-1} in science acquisition mode, and 5×10^{-4} photons pix^{-1} sec^{-1} in other acquisition modes, the pixel's charge capacity must be considered in order to avoid unwanted saturation in the high gain register should a bright source spuriously contaminate the field. Other factors such as charge persistence must be considered in such scenarios.

5.5.2 Persistence

Persistence can occur when there is residual charge trapped in the surface or bulk regions of an EMCCD, and typically occurs if the device has been over-exposed to light such that the pixel charge capacity is exceeded. There are two main types of persistence, also known as "residual image": (1) residual surface image (RSI) and (2) residual bulk image (RBI).

RSI can cause signal charge to get trapped in the Si–SO2 interface, which may persist at these positions and subsequently get released during a readout. Charge trap lifetimes can be long and so persistence can be seen for hours or weeks after it occurs.[22] However, the use of IMO in the CCD201 eliminates surface trapped charge immediately by flooding the Si–SiO2 interface with holes; therefore, the RSI component is eliminated. In parts of the CCD that are never inverted, such as the high-gain register, RSI is a potential issue. However, the high-gain register pixel well capacity is much larger than the image/store pixel well capacity, so it is unlikely that charge will ever reach the surface under normal, unbinned operation. In order to investigate potential damage or persistence effects, testing is currently ongoing at JPL, where EMCCDs are being subjected to the highest predicted signal levels from a CGI observing mode. In the event that the high-gain register becomes saturated, it has a built-in mechanism to prevent overloading from occurring.

Vertical antiblooming in a device can negate the effects of RBI; however, there is no vertical antiblooming in the CCD201. With back thinning, RBI is reduced compared to front-illuminated CCDs because the epibulk interface is eliminated by the thinning process. However, a small amount of RBI remains, from unknown sources.

5.5.3 Mode of operation and cooling

Since the CCD201 contains two boron barrier implants under two of its phases, it can be clocked in IMO. In this mode, the substrate voltage (V_{SS}) is raised to a level higher than that of the potential at the semiconductor–insulator interface beneath the gate electrodes. Once this condition has been fulfilled, holes migrate from the channel stops of the device to the semiconductor–insulator interface and populate the traps that are present due to the atomic mismatch between Si and Si–O2. Since the traps are populations with holes, dark current generation from this region is significantly reduced. Therefore, IMO is favored over NIMO, and by using IMO for the CGI application, which includes individual integration times of order 100's of seconds and accumulated total integration times of several 1000 s, the dark current requirement of 5×10^{-4} e$^-$ pix^{-1} sec^{-1} can be achieved at and below temperatures of -85° C. In flight, we expect the sensor to be passively cooled with active warming.

Although running the device in NIMO can greatly reduce CIC, as stated previously, dark current accumulation is likely too high in this mode. We would need to use temperatures of approximately 115° C and below to sufficiently suppress the dark current in NIMO; however, under high gain, we are still investigating if temperatures in this range will cause increased CTI. In the following section, we describe recent work that has been carried out at the manufacturing system level that offers lower parallel CIC.

5.5.4 Clock induced charge minimization

CIC is highly dependent on the clocking process,[22] and therefore at the camera system level, custom clocking parameters, including careful consideration of V_{SS}, clock swing, and clock amplitude, can be considered to minimize these effects. We note that other groups claim that wave shaping can also play an important role in CIC minimization.[31] These efforts are ongoing at JPL to achieve similar spurious noise contribution at lower horizontal read out rates. Since CIC levels are affected by clock amplitude, and since the CIC will rise exponentially with the clock amplitude[52] under EM gain, it follows that lower clock amplitudes will produce lower CIC. There is a minimum voltage that must be used in order to move charge in the parallel section; however, as a result of the barrier implants described previously, a fixed potential is present in the silicon and any charge must overcome this static field in order to maintain sufficient device charge transfer. In recent work by Gach et al.,[33] they outline a strategy to reduce the effective implant dose of an EMCCD (CCD282), consequently lowering the required clock amplitude to maintain charge transfer. Impact ionization is therefore reduced in the local electric field. This reduction in implant dose will also mean a reduction in the FWC of the device; however, a tradeoff between dose reduction and FWC is dependent on the application. This modification could also be applied to the CCD201 and might be considered if CIC levels become problematic. Additionally, increasing the number of multiplication elements (N) would result in the same given gain factor (G) being achieved by using a lower gate high voltage, since $G \propto N$, as previously shown in Eq. (1). By producing lower EM gain, less impact ionization would occur due to lower electric fields thus reducing CIC. The CCD201 has 604 multiplication elements in its standard design, and therefore this would require a further design change.

Another way of reducing parallel IMO CIC to NIMO CIC levels is via multilevel clocking of the image/store array (see Murray et al.[53] for discussion of such clocking techniques). During an integration, all of the clocks are held low enough with respect to V_{SS} so that the image array is fully inverted. After this integration, but before the image to store transfer, the low rail of the image/store clocks is raised (or alternatively, V_{SS} is dropped) enough so that the image/store array is taken out of inversion. The device is therefore readout in NIMO mode. At higher temperatures than -108° C (165 K), NIMO dark current may no longer satisfy CGI requirements. Once the CGI operating temperature has been selected such that the dark current and CTI are minimized under high gain, this optimization can be considered further.

5.5.5 Clocking considerations: charge transfer inefficiency

CTE is defined as the efficiency of a device to transfer charge from one pixel to the next and is an extremely important parameter that affects a CCD's overall performance, where CTE = 1 – CTI. CTI can vary based on the vertical clocking frequency, wave shape, and horizontal frequency, in addition to the temperature of the

device with high multiplication gain (and because of radiation damage, see Sec. 6). Indeed, by designing custom clock signals in an attempt to minimize other sources of noise, e.g., CIC, the CTI can be adversely effected, see, e.g., Murray et al.[53] and Hall et al.[38] The data presented in this section was produced by using the CCCP version 3 controller,[54] which has been designed to minimize both vertical and horizontal CTI for photon counting applications that can yield CTI of order $\sim 1 \times 10^{-5}$. This controller has a core operating frequency of 240MHz and produces 4.16-ns time resolution for all analog signals. Digital CDS can process up to 2048 samples per pixel. It generates 14 analog clocks (± 15 V) where two high-voltage clocks, with resonant frequencies of 10 and 20 MHz with 68- ps resolution, are used. The CCCP therefore generates clock and bias signals with precision timing and produces low dark current (run in IMO) and low CIC (clocking architecture), while maintaining sufficient charge transfer

As discussed in Sec. 4, the CCD201 will undergo radiation damage in the WFIRST orbit, and therefore a clocking design that is sufficient to deliver the required CTI performance at BOL might not be applicable as damage accrues over the mission lifetime. Clocking strategies will therefore be required to identify damaged sites on the sensor, as well as additional techniques to mitigate this damage and/or maintain charge transfer quality under irradiated conditions. The performance of devices, as shown in, e.g., Daigle et al.,[31,54] Gach et al.,[33] and the strategies used to obtain the resulting S/N, have yielded extremely promising results for devices at BOL. These strategies and techniques are being developed further at JPL specifically for irradiated CCD201s to meet the CGI requirements at EOL. Details of this work will be published in a separate document at a later time. In Sec. 6, we outline some preliminary clocking techniques that were designed as a tool to investigate displacement damage in the CCD201.

5.5.6 Manufacturer design modifications

After selection of the CCD201 for the WFIRST-CGI, in addition to the performance differences between a standard thickness silicon device and a deep depleted device (see Sec. 1.2), we also considered design modifications at the device processing level that could yield higher S/N performance. Two main modifications were considered: (1) reducing the channel width of the device and (2) reducing the device's barrier implant dose.

A reduction in the channel width would reduce the charge store volume of the image and store sections. This would have the effect of reducing the amount of trapping sites that a charge cloud could interact with during readout, thus decreasing the CTI. We note that discussions with e2v have suggested that this is considered to be a nontrivial design change. Reducing the implant dose under phases 1 and 3 of the CCD201 would yield negligible levels of CIC in the parallel section;[33] however, a tradeoff between implant does reduction and a similar reduction in FWC must be considered. Importantly, by completely removing the implant, IMO would no longer be possible, which would affect the dark current.

Since the standard off-the-shelf CCD201 has higher maturity and lower fabrication risk than a custom design, we decided to implement no manufacturer design modifications at this time and baselined the standard device for the WFIRST-CGI. Although it is not desirable to propose modifications to a sensor that has been selected based on its maturity, if EOL performance as indicated by the radiation phases I and II test plans does not meet the CGI requirements to the point that the CCD201 can no longer provide sufficient planetary yield for the mission, then these modifications will be reconsidered as well as substitution of other flight-rated conventional CCDs.

6. RADIATON STUDY OF CCD201-20

6.1 Test Plan and System Calibration

6.1.1 Phase I irradiation plan

In Sec. 1, we outlined a two-phase radiation study to investigate DDD damage on the performance of the CCD201. In this section, we present the results of phase I, where an ambient temperature, unbiased, irradiation was carried out at the proton irradiation facility (PIF), at the Paul Scherrer Institute (PSI), in Switzerland, on February 23, 2015, and postirradiated analysis was carried out at CEI, in the United Kingdom. This study was designed to include full sensor characterization of two engineering grade CCD201 devices at ambient temperature. It should be noted that although these devices are considered engineering grade, we consider the measured performance

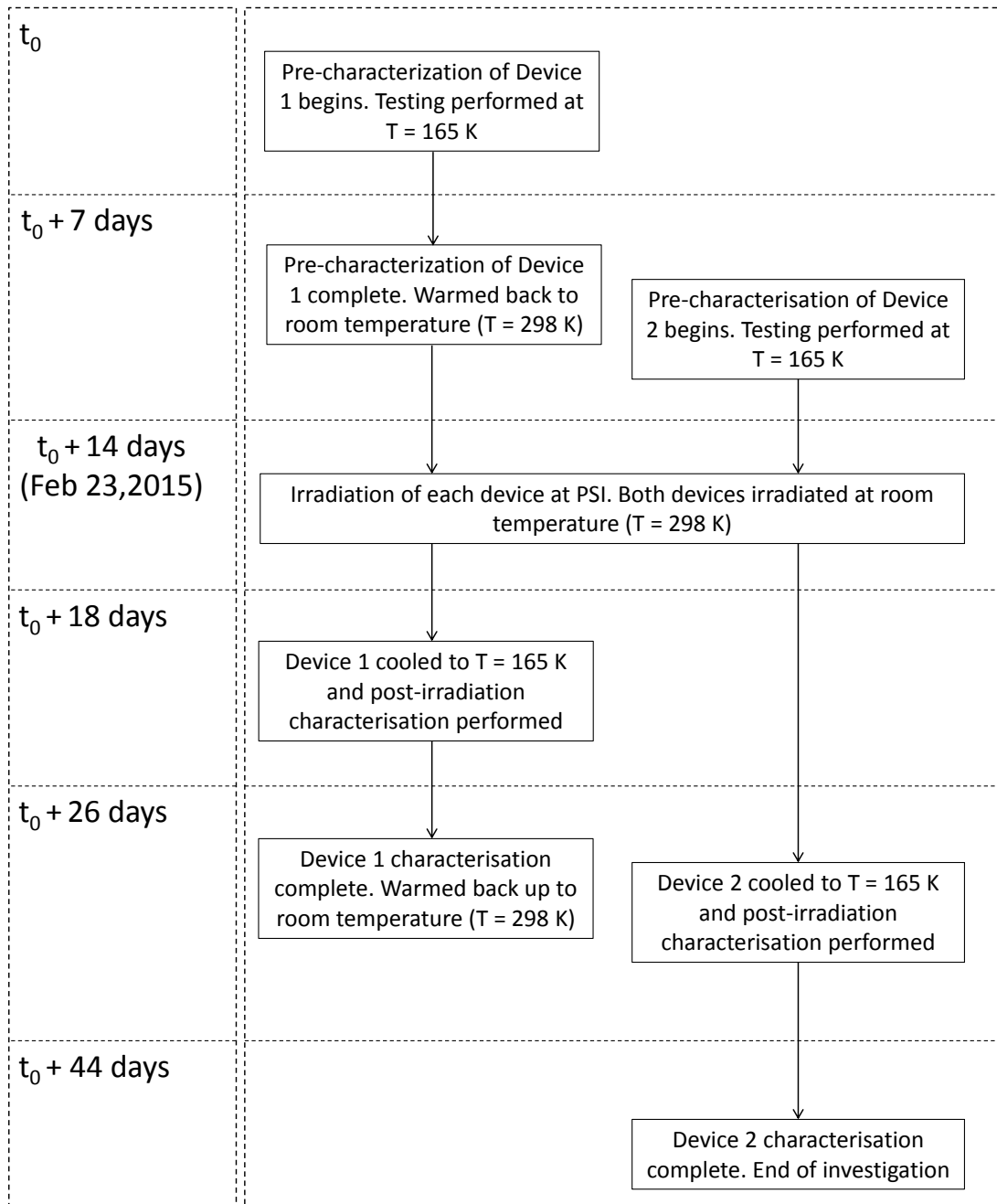## Radiation Phase I Detector Test Flow Schematic

t_0	Pre-characterization of Device 1 begins. Testing performed at T = 165 K
$t_0 + 7$ days	Pre-characterization of Device 1 complete. Warmed back to room temperature (T = 298 K) — Pre-characterisation of Device 2 begins. Testing performed at T = 165 K
$t_0 + 14$ days (Feb 23,2015)	Irradiation of each device at PSI. Both devices irradiated at room temperature (T = 298 K)
$t_0 + 18$ days	Device 1 cooled to T = 165 K and post-irradiation characterisation performed
$t_0 + 26$ days	Device 1 characterisation complete. Warmed back up to room temperature (T = 298 K) — Device 2 cooled to T = 165 K and post-irradiation characterisation performed
$t_0 + 44$ days	Device 2 characterisation complete. End of investigation

Figure 12. Radiation phase I detector test flow diagram. The left column of the schematic shows the beginning of the test, t_0, where we include each major step in the program until the end of the test, $t_0 + 44$ days. The right column shows each subsequent stage of the program for each device, including when the radiation occurred as well as details of timings, cooling, and temperatures.

in this study postirradiation as representative of what scientific grade sensors will experience, since this study sought to investigate a degradation factor on performance for each characterization parameter. These parameters include multiplication gain, dark current, CIC, high flux parallel and serial CTI as well as low flux parallel and serial CTI, before and after a radiation dose of 2.5×10^9 protons cm^{-2} (10 MeV equivalent). This dose reflects the EOL dose (6 years in L2) for a 10-mm tantalum shield. We show a detector test flow diagram in Fig. 12. Phase II commenced in June 2015 and covered the full range of doses for all of the shielding materials and thicknesses shown in Fig. 6, where a custom apparatus was designed and built to maintain device cryogenic temperatures throughput the study.

We selected irradiated regions of each device thereby ensuring a control region for both parallel and serial registers–this allowed the independent and combined effects of radiation-induced displacement damage on parallel and serial CTI to be investigated in a meaningful way that prevented contamination. A schematic of this control scheme is shown in Fig. 13. Monte Carlo simulations were performed using the Stopping Range of Ions in Matter package (SRIM).[55] These simulations provided the maximum penetration depth of the beam as it passes through stainless steel (the element used for shielding), which was ∼9 mm, thus a thickness of 14 mm was used for redundancy.

For device 1, the shielding profile was designed such that the degradation of parallel performance could be evaluated where serial and high-gain registers were protected. Additionally, the right side of the parallel section was also protected and used as a control region, where results from this section were expected to be identical to those prior to irradiation. The shielding profile in device 2 allowed the effects of radiation damage to be assessed on both the serial and parallel sections, as well as these sections combined. In this way, charge getting transferred through the right side of device 2 should get affected in the serial direction only. Note that in device 2, a small region of the parallel section in the control region (right side) was irradiated; this is because the serial register is small when compared to the store and image sections, and therefore irradiating a small region (∼300 pixels) of the parallel section ensured that the serial register was fully irradiated.

6.1.2 Device parameters and calibration

CCD controller. All pre- and postirradiation tests were carried out at -108° C (165 K) with a frame integration time of 100 s (unless otherwise stated) and the devices were run in IMO. The CCD was operated using generic drive electronics for test and characterization from XCAM Ltd.,[56] consisting of a 19″ inch rack-based controller, together with proximity electronics on a headboard PCB local to the CCD, providing bias filtering and low noise preamplification. The control electronics used for testing were standard and thus were not fully optimized to match those of the EMN2 described earlier in Sec. 5. We note that the use of this controller does not invalidate this test, since we sought to identify performance degradation of the CCD201 only– this does not include controller or other proximity electronics. While some parameters will change based on the camera controller used (e.g., readout rate), the trends exhibited due to radiation damage in this study should be independent of the CCD controller. Part of the study strategy was to keep pre- and postirradiation controller operating conditions identical. We felt that it was important to initially separate the detector and the controller so that we could interpret results in the context of the EMCCD only. The EMCCD flight electronics will be designed for performance in the relevant environment.

Calibration. The XCAM setup enabled rapid investigation of the pre- and postperformance of the device. We used the default readout modes for clocking through the LS amplifier and bias signals as recommended by e2v[48] were used with the device image and store sections being operated in two phase mode. Some minor modifications were made based on precharacterization tests in order to minimize the readout noise and a read out pixel rate of 700 kHz and parallel line transfer time of 6 μs per phase were employed. We used the drive system with the option of XCAM's two-channel CDS card, where with the combination of headboard gain and CCD output node responsivity, the system noise for EM gain = 1× is dominated by the noise on the 14-bit ADC (rather than the CCD itself). However, operating with a maximum amplification gain of ∼200, we were able to routinely operate with an effective readout noise of 0.8 e$^-$ rms. This low effective noise was important in order to minimize the CTI (from both small optical signals and ^{55}Fe x-rays) within the multiplication register. Once optimized, we kept these bias conditions consistent for pre- and post-analyses. Similarly, the same Rϕ2HV (this voltage controls the multiplication gain) was consistent in both scenarios.
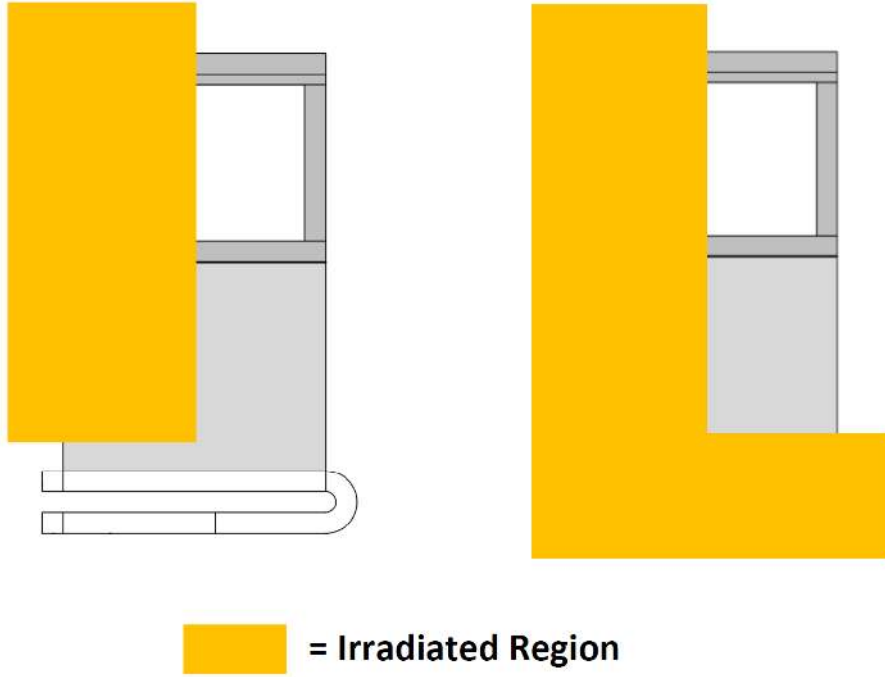
31

Device 1: 10091-16-09   **Device 2: 11153-13-14**

= Irradiated Region

Figure 13. Irradiation pattern for each CCD201 device. We note that the relative size of the serial and multiplication registers is not to scale in this image. For device 1, the shielding covered the first ∼300 pixels of the store section, as shown, in order to prevent any effects of secondary nuclear interactions in the proximity of the shielded edge.

The amplifier responsivity and conversion gain were measured in order to calculate the system calibration, DN/e^-, as follows:

$$\frac{DN}{e^-} = \frac{V}{e^-} \cdot \frac{DN}{V}, \tag{5}$$

where V/e^- is the amplifier responsivity and DN/e^- is the k-gain. We note that DN/e^- is the system calibration^{-1}. This calculation was necessary since it provided the signal level as measured from the phase I device and system electronics and was essential for measurements later. Obtaining these parameters prior to irradiation was also a good indication of a change to the output electronics after the radiation tests were carried out. An ^{55}Fe x-ray source was used for this component of calibration.

6.2 Proton Fluence and Beam Profile

In order to achieve a proton fluence of 2.5×10^9 protons cm^{-2} (10 MeV equivalent), we used the PIF at PSI, Switzerland, which was been used by ESA for major testing of spacecraft components. The key features of the facility that allowed this radiation dose to be achieved are as follows:

- **Lowest initial proton energy:** 74 MeV.

- **Beam profile:** Gaussian with typical FWHM of 10 cm.

- **Neutron background:** $< 10^{-4}$ neutrons proton^{-1} cm^{-2}.

As indicated previously, since the lowest primary beam energy at PSI is 74 MeV, we needed to extrapolate the final dose required at 74 MeV to deposit equivalent energy levels into the CCD201s, as a 10-MeV beam at the required fluence. We therefore adopted the Non Ionizing Energy Loss (NIEL) function, as found in Burke et al.,[57] Vanlint et al.,[58] and Srour et al.:[59]

$$10 \text{ MeV NIEL Function} = \frac{1.6}{E_p^{0.28}}, \tag{6}$$

$$10 \text{ MeV NIEL Function} = 0.479, \tag{7}$$

$$\text{Fluence at 74 MeV} = \frac{2.5 \times 10^9}{0.479}, \tag{8}$$

$$\text{Fluence at 74 MeV} = 5.21 \times 10^9 \text{ protons cm}^{-2} \tag{9}$$

Prior to irradiation, the intensity of the PIF beamline was mapped around the target area to confirm that the beam intensity across the irradiated regions was consistent with the above calculation in Eq. (9). A normalized beam intensity difference of <8% was measured from the center of the CCD201 (where the image and store sections meet) to the outer edge of the device (top of image section and bottom of serial section), which we found to be sufficient for this study.

6.3 Trap Pumping: Initial Identification of Damage

Although the majority of trapping sites in an irradiated device are a direct result of displacement damage, some traps will be present as a result of imperfections caused during the manufacturing process, e.g., poor cleaning between the silicon base and the first polylayer is a big factor in the number of these so-called "design traps". Such sites were therefore assessed prior to and postirradiation in order to (1) highlight the irradiated regions (where new traps now exist) and (2) determine the approximate trap density and distribution in the device.

Standard pocket pumping[22] was employed, which provides the means of probing trap sites, where pixels were clocked in the forward direction and then subsequently in the opposite direction. We highlight again that since the CCD201 device is designed to be operated in a two-phase mode with charge only flowing forwards, each of the four phases is independently connected and therefore the device can be operated as a four phase device, albeit provided that one considers the impact of the implants on the clocking. To do this, we paired $\phi 1$ and $\phi 2$ together and $\phi 3$ and $\phi 4$ together, to push charge forward, and then paired $\phi 2$ and $\phi 3$ and $\phi 1$ and $\phi 4$ together, to push the charge backward. This technique was then repeated, which transfers charge between adjacent gates within the same pixel and thereby captures traps within the signal packet which are then released into a neighboring pixel when the original signal packet has moved from the trapping location. As a result of this process, a pair of bright and dark pixels is now present signaling a trapping site and can otherwise be known as a "dipole". Note that all of the trap populations will not be present as a result of the pumping cycle described above. This is because trapping efficiencies are a function of temperature and also parallel line transfer timing, and each pumping cycle will only probe a certain area of the pixel. Furthermore, the pocket pumping technique used to generate the images as shown in Fig. 14 did not probe 100% of the pixel, where we estimate <50% was probed; this is a tentative estimate since it is difficult to know the effect of fringing fields within a pixel. Work is ongoing to probe a larger area of the pixel, which is difficult based on the presence of barrier implants.

We show the results of this analysis in Fig. 14, where new dipole populations are clearly evident and in greater number as a result of displacement damage. We cannot offer a %-increase in population at this time, since many pocket pumping iterations are required to probe disparate trapping efficiencies, as outlined above. We refer the reader to Hall et al. (2014),[23–25] Wood et al (2014),[26] and Murray et al. (2012)[27,28] for in-depth studies of trap pumping for radiation-damaged devices.

Device 1: Parallel Irradiation **Device 2: Parallel & Serial Irradiation** **Comparison of traps Pre-/post-irradiation**
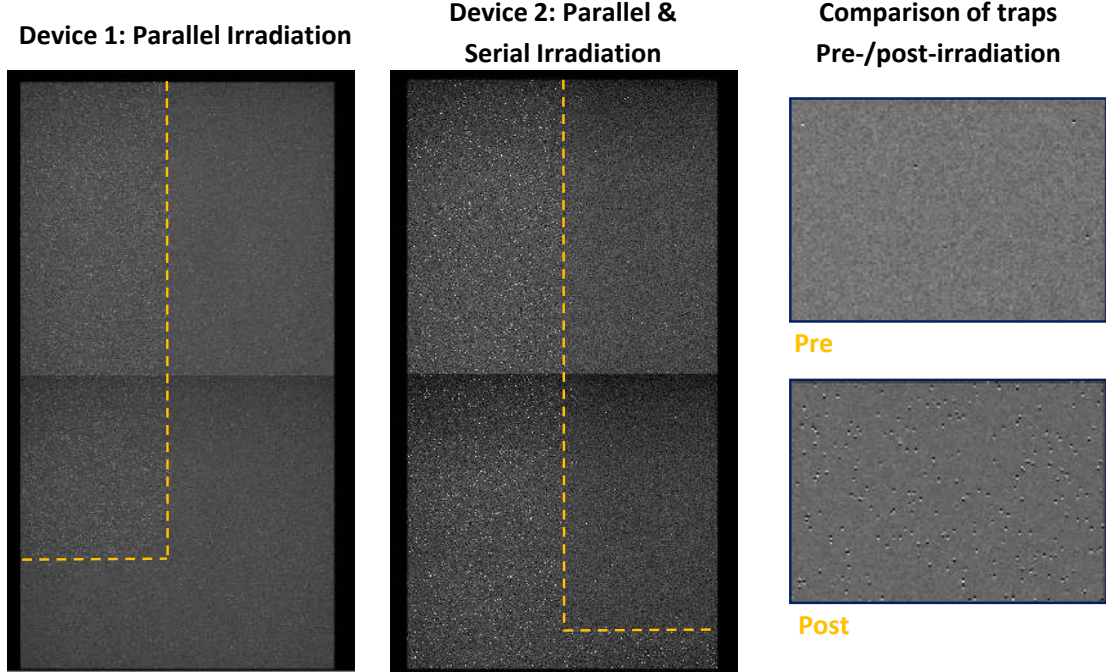
Pre

Post

Figure 14. Basic pocket pumping that was carried out in order to highlight the unirradiated and irradiated regions of device 1 (left) and device 2 (center). We also show a comparison trapping site (right), highlighting a region of 90×50 pixels in the image area. In all cases, it is clear that the irradiated regions (within the dashed boxes) contain a much higher density of dipoles.

6.4 Results: Pre- vs. Post-Irradiation

Here, we present displacement damage radiation results for the CCD201. This is the first study to be carried out with a CCD201 in assessing performance degradation of this kind. We can confirm that both CCD201 EMCCD devices were fully functional after irradiation and experienced the degree of degradation in multiplication gain, dark current, CIC, and charge transfer that has been previously reported by other CCD sensors[59] irradiated to a similar dose. We summarize the key performance degradation below and show comparison results for each device in Table 9:

- Each device was fully functional following irradiation to 2.5×10^9 protons cm^{-2} (10 MeV equivalent).

- No significant change in the multiplication gain was observed (for an unbiased irradiation at ambient temperature).

- No significant change in the parallel CIC was observed (for an unbiased irradiation at ambient temperature).

- There was an IMO dark current increase by a factor of $\sim$2.

- For low signal parallel CTI ($\sim$8 e$^-$), there was a degradation by a factor of $\sim$5. The serial CTI appears to be dominated by the EM register and interaction with surface states for the operating conditions that were used.

- Initial results suggest that serial CTI of the EM register has some dependence on the size of the signal being transferred as well as values for ϕDC and Rϕ2HV.

Table 9. Summary of pre- and post-irradiation test results for both CCD201 EMCCD devices. Any degradation factor that is left blank we consider to be inconsistent.

Parameter	Device 1 Pre-Irradiation	Device 1 Post-Irradiation	Device 2 Pre-Irradiation	Device 2 Post-Irradiation	Degradation [factor]
Multiplication Gain	238 ± 7	202 ± 6	237 ± 8	237 ± 8	...
Eff. Read Noise (e^- pix^{-1})	0.85 ± 0.04 [Par.]	0.98 ± 0.06 [Par.]	0.70 ± 0.07 [Par. + Serial]	0.91 ± 0.04 [Par. + Serial]	$\sim$1.2
Par. I_{DK} (e^- pix^{-1} sec^{-1})	(7.13 ± 0.49) $\times 10^{-5}$	(1.22 ± 0.06) $\times 10^{-4}$	(3.195 ± 0.50) $\times 10^{-5}$	(5.75 ± 0.44) $\times 10^{-5}$	$\sim$1.8
Par. CIC (e^- pix^{-1} fr^{-1})	(4.47 ± 0.24) $\times 10^{-2}$	(4.86 ± 0.26) $\times 10^{-2}$	(8.80 ± 0.38) $\times 10^{-3}$	(9.90 ± 0.10) $\times 10^{-3}$	...
^{55}Fe Par. CTI	(5.14 ± 3.90) $\times 10^{-6}$	(4.05 ± 0.54) $\times 10^{-5}$	(1.23 ± 0.59) $\times 10^{-6}$	(3.07 ± 0.08) $\times 10^{-5}$	$\sim$10
^{55}Fe Serial CTI (Conv. register)	(1.05 ± 1.36) $\times 10^{-6}$	(2.04 ± 2.66) $\times 10^{-6}$	(1.73 ± 1.49) $\times 10^{-6}$	(1.08 ± 0.67) $\times 10^{-5}$	...
^{55}Fe Serial CTI (EM register)	$(1.19 \pm 0.01)^{\dagger}$ $\times 10^{-4}$	$(6.82 \pm 0.01)^{\dagger}$ $\times 10^{-5}$	(1.69 ± 0.01) $\times 10^{-4}$	(1.83 ± 0.01) $\times 10^{-4}$	$\sim$1.12
EPER Par. CTI	(1.13 ± 0.20) $\times 10^{-4}$	(5.40 ± 0.80) $\times 10^{-4}$	(9.26 ± 0.70) $\times 10^{-5}$	(3.94 ± 0.45) $\times 10^{-4}$	$\sim$5
EPER Serial CTI	(2.37 ± 0.70) $\times 10^{-4}$	(2.06 ± 0.22) $\times 10^{-4}$	(1.73 ± 0.21) $\times 10^{-4}$	(2.32 ± 0.38) $\times 10^{-4}$	...

†Device 1 did not have the EM register irradiated. However, the CTI has been reduced by a factor of $\sim$1.7. This may be because of a decrease in multiplication gain that was observed for the device during post-irradiation testing. The total amount of signal would thus be smaller passing through the EM register and so less interaction with surface traps would occur. Acronyms/abbreviations: Par. = parallel; CTI = Charge Transfer Inefficiency; EPER = Extended Pixel Edge Response.

6.4.1 Multiplication gain and read noise

Multiplication gain. The multiplication gain was measured in the same way as system calibration, by using an ^{55}Fe source where the Rϕ2HV voltage was varied. The gain was found for each voltage by normalizing the system calibration gain to that with a unity gain. The multiplication gain behaved as expected where we observed a measured gain with an exponential rise with respect to the applied Rϕ2HV clock. The gain profile remained consistent for both devices before and after radiation testing. We measured no difference (within error) of multiplication gain for device 2, where we found values of 237 ± 8, prior to and after radiation exposure. The serial register was irradiated for this device, therefore, based on this result, it appears that this level of fluence does not have an effect on the multiplication gain for a room temperature, unbiased irradiation. However, we note that if a causal flat-band voltage shift were to occur as a result of such exposure, it could affect this result.

Interestingly, device 1 had a measured decrease in its multiplication gain, even under a consistent Rϕ2HV clock voltage. This device was not subjected to any radiation exposure in the serial register; therefore, this discrepancy cannot be attributed to such effects. One plausible explanation is that device aging might have caused degraded gain. This phenomenon can occur due to the buildup of charge carriers under the Rϕ2HV electrode or the ϕDC electrode. Although e2v condition their devices prior to release, the so-called "burn-in phase", it is possible that aging could be responsible since the multiplication gain for a given Rϕ2HV voltage can decrease as a device is continuously used. Aging will affect a device the most in the first $\sim$10 h of life; however, some latent effects might still be present. Finally, we note that a larger Rϕ2HV voltage was used for device 1 when compared to device 2. Even the smallest increase in voltage in the high-gain register can cause significant changes in amplification gain thereafter. Therefore, other transient effects would be observed in device 1 before the same effect might be observed in device 2. We are currently investigating this further.

Read noise. For this setup, the read noise of the CCD201 was found in a similar way to that outlined in Sec. 5.2, where the 16 prescan elements (prior to the high-gain register) were used. Although these pixels will still contain some dark current and some CIC that has been amplified by the gain register from the previous line readout, these components were removed by backclocking the prescan elements before the line readout for a given frame. A histogram of the signal as a function of DN can then be used to find the read noise where a Gaussian curve is fitted and the mean is calculated.

For devices 1 and 2, the readout noise was observed to increase. As outlined in the previous subsection, since there was a measured decrease in the multiplication gain of device 1, this might account for a subsequent increase in effective read noise; however, since there was no measurable change in device 2's multiplication gain, this explanation is not consistent for both devices. Since device 2 was subjected to radiation exposure in both the parallel and serial registers, dark current generation in the serial register might have contributed to this increase. However, measures were taken to minimize dark current in device 2 by the back-clocking procedure described above. Indeed, the stability of the EM process, and in turn the multiplication gain and the read noise, all rely on careful control of the electronics and device conditions throughout an integration. Radiation damage can complicate this equilibrium. As before, investigations are ongoing.

6.4.2 Dark current (inverted mode operation)

Long integration frames were obtained in the range 300 to 3600 s in order to measure dark current. CRs were removed from the data as before, and parallel and serial CIC was removed by using regions of the parallel overscan. The mean value over a range of pixels in the image and store regions were then used to calculate dark current in the parallel section. This was performed pre- and postirradiation, and the results of this study are shown in Figs. 15 and 16.

In each case, the measured dark current preirradiation was of order 10^{-5} e$^-$ pix^{-1} sec^{-1}, where tests were performed at -108° C (165 K). Note that in the beam line, the sensor was at ambient temperature and thus some of the subsequent damage from displacement events was annealed out. The second phase of this radiation study will irradiate under the same temperature at all points of the study; this is outlined further later in this section. Dark current was a factor of $\sim$1.8 higher for each device after displacement damage had occurred. We highlight that device 1 was measured to have higher dark current than device 2. This can be explained based on a classification of engineering grade due to high dark current upon release from e2v. Therefore, device 2 is likely
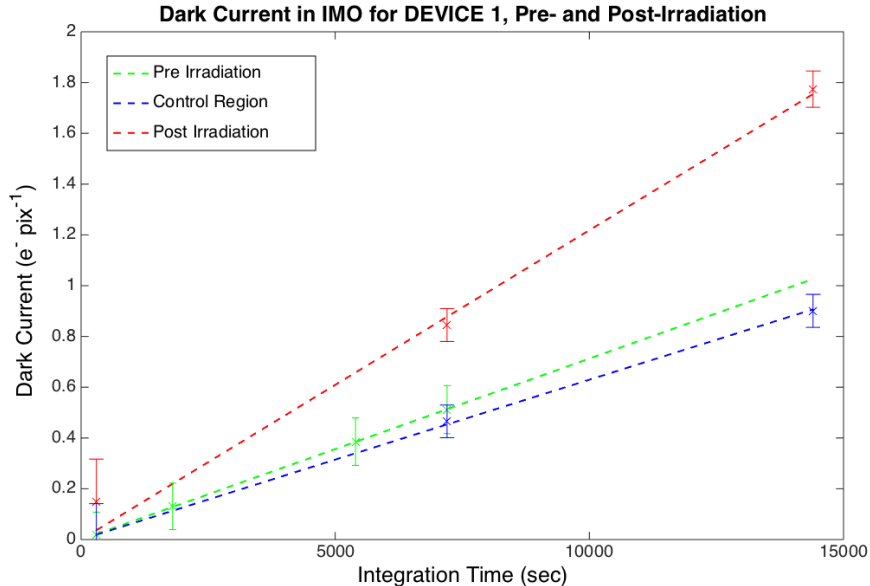
Figure 15. Plot of dark current (e^- pix^{-1}) as a function of integration time (s) for device 1 showing pre- and post-irradiation in addition to the control region. We set the intercept to zero in order to assess clearly the trends for pre- and post-irradiation data.

more representative of what a science-grade device would undergo in orbit. We note further that although each device was measured in IMO, in this mode, the dark current can be heavily dependent on the applied V_{SS}. As outlined previously, we used standard CCD201 data sheet values for this experiment. However, as noted in Fig. 10, the dark current in this setup is consistent with the dark current trend from the highly tuned EMN2 system that was used for sensor characterization of CGI requirements.

6.4.3 Clock induced charge

Parallel clock induced charge. Based on methods developed by e2v, parallel CIC was measured by using a customized sequencer. This is where a single line of signal is created in the serial register by clocking a large number of rows. This signal is then read out of the device, which is predominantly made up of CIC. After this process, the device is subjected to a frame integration time equal to the time taken to read out the number of rows in the previous process. In this time, dark current will accumulate, and these pixel rows are binned and also read out. As a result, there are now alternate lines of dark current + CIC, and dark current alone, for the same time interval. By calculating the difference between these signals, the parallel CIC can be found.

A mean CIC value for each device was calculated by averaging these rows and then dividing by the number of parallel transfers. We obtained CIC measurements for different values of clock swing. The clock swing is the difference between the high and low values in the image and store clocks. CIC is heavily dependent on this parameter (based on higher local electric field conditions for varying clock swing), but in this work, we present pre- and postirradiation results for the lowest CIC only. For both devices, the difference in CIC is very small, as shown in Table 9. The expectation prior to the radiation test was that CIC would not be affected by displacement damage since the mechanism for the creation of CIC should not get affected in this way. Trap sites are not responsible for the capture and emission of holes during CIC generation; this happens within the clocking process.We note that flat-band shifts should be considered for device optimization, since any shifts of this kind in flight would affect the derivation of the V_{SS} value, which can have a big effect on both dark current and CIC. Indeed, the pinning potential, which refers to the V_{SS}, can vary from device to device and thus different voltages may be present. This might explain the discrepancy between the CIC measured in devices 1 and 2, where CIC in device 1 was measured to be higher.
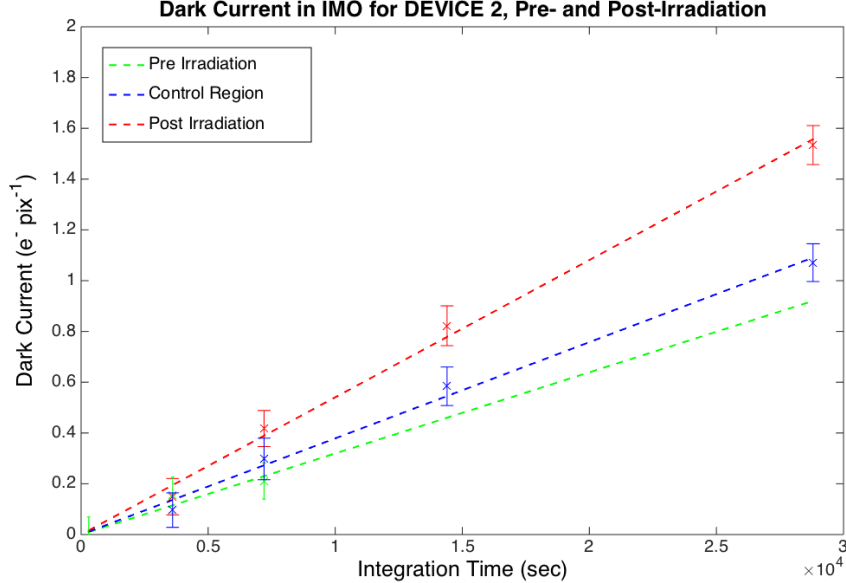
37

Figure 16. Plot of dark current (e^- pix^{-1}) as a function of integration time (s) for device 2 showing pre- and post-irradiation in addition to the control region. As before, we set the intercept to zero in order to assess clearly the trends for pre- and post-irradiation data.

Serial clock induced charge. By considering the method for calculating parallel CIC, the time taken to bin columns to the output node was too long for the allowable CDS sampling cycle of the control electronics; therefore serial CIC could not be measured in the same way.We measured serial CIC as before, in Sec. 5.4, by using the serial overscan in the images. This value was then scaled by the system calibration measurements to calculate CIC alone. However, we discovered some contribution from other on-chip sources during this process (both pre- and postirradiation) and do not consider the current analysis using the test camera system to be providing representative values for serial CIC alone. Investigation showed that this was a phenomenon likely exacerbated by the camera system. We made sure to confirm that the methods used to calculate other performance figures take the noise into account and are unaffected.

6.4.4 Charge transfer inefficiency

^{55}Fe *X-rays: high flux charge transfer inefficiency.* CTI for high flux was measured using a ^{55}Fe x-ray source by taking 50 images with integration times of 100 s at -108° C (165 K). The x-ray density was $\sim$1 event per 200 pixels. Regions of the sensor were assessed independently and the average value of all single events in these regions was evaluated and plotted as a function of pixel position in either row or column, depending on whether parallel or serial CTI was being assessed. A fit was applied to these data and the gradient of this fit was used to calculate a value for CTI; the uncertainty in this derivation was taken to be the standard deviation of single events within a region. Both the conventional register (unity gain) and the EM register were used to confirm that CTI was the same in both cases (as expected). In Table 9, we show these measurements.

As expected, devices 1 and 2 have shown increased CTI as a result of displacement damage, the CTI measurements in the control regions are consistent with the measured CTI in any preirradiated region. We found no significant degradation of the conventional register in device 1 (register was shielded), whereas device 2 showed a measured decrease as a result of the radiation dose, as expected, where we measure a factor of $\sim$1.12 increased CTI in the EM register. We note that in order to calculate the CTI in the EM register, some assumptions must be made since the signal is changing as it moves through the amplification process. These are (1) the CTI of each multiplication element is the same and (2) the deferred tail, explained below, accounts for most of the lost charge. Additionally, CTI in the EM register will be dependent on the Rϕ2HV and ϕDC values, in addition to how much charge is present, the system temperature and the gain applied.
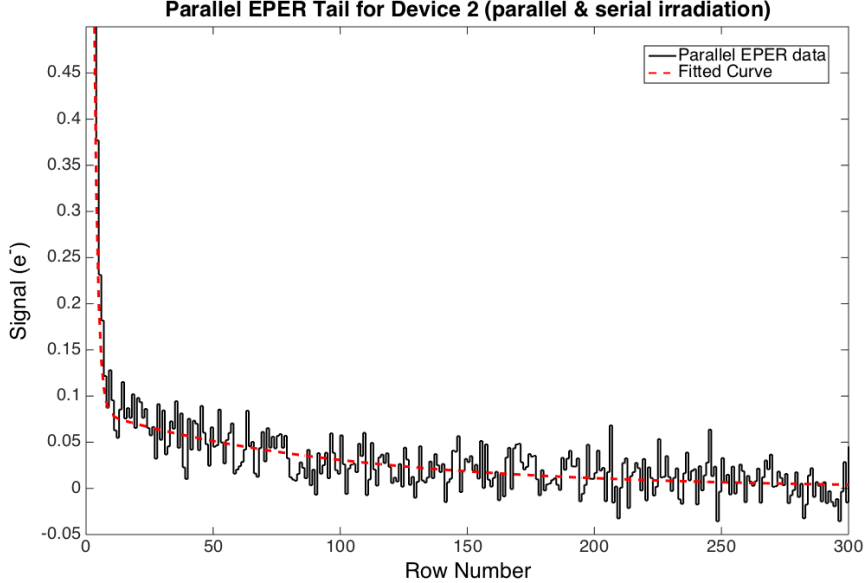
Figure 17. Parallel EPER tail for device 2 (parallel and serial irradiation). The first 300 deferred pixels are shown. The fit consists of two exponential functions, where fast traps emitted in the first $\sim$10 pixels are fitted first then slower traps that are emitted some time later. By integrating under the curve, the total charge emitted can be found, which is $\sim$8 e$^-$.

To measure the deferred charge tail, images were once again measured using a ^{55}Fe x-ray source, with integration times of 100 s at -108° C (165 K). A histogram of the image was created in order to identify single events, located at the Mn-Kα peak (located by fitting a Gaussian). $\pm 2\sigma$ limits were applied to the fit, and events within this range were classified as single events. All events were summed and averaged to estimate a mean value, which helped to reduce the noise as a result of the ENF from the multiplication process. The total deferred charge tail was summed and used in the following equation[54] to calculate the CTE in the EM register (we found the CTE via the following equations and then converted to CTI as previously outlined, where CTE = 1 – CTI):

$$CTE_{HV} = (1 - E_{def})^{\frac{1}{N}}, \tag{10}$$

where E_{def} is the deferred charge tail and N is the total number of multiplication elements in the CCD201, which is 604. Crucially, much like CIC, the values for CTI obtained from this experimental setup do not reflect those required for the CGI. As previously stated, the appropriate considerations of the Rϕ2HV and ϕDC voltages, in addition to the operating temperature, are all very important in minimizing the CTI of a device. This study aimed to investigate degradation based on displacement damage only.

Extended pixel edge response: low flux charge transfer inefficiency. Low signal CTI, most applicable to the WFIRST-CGI, was measured using the extended pixel edge response (EPER) technique, see Janesick[22] for more details. As before, we first find CTE and then convert to CTI. EPER uses a flat field where the CTE is estimated by measuring the amount of deferred charge found in the serial or parallel overscan regions, defined as the line region (or "extended pixel" region). The technique is based on the sharpness of this edge and interpreting the results in terms of traps in the detector causing degradation of charge transfer. If charge transfer, as characterized by CTI is poor, large amount of charge from the illumination get captured by traps and subsequently re-emitted when the charge cloud is transferred. The drop in signal is known as a "deferred charge tail", which arises from this process. If the charge transfer was perfect, there would be no deferred charge, and a "square wave" edge would be present in the EPER data. Since traps result in some of the charge being deferred, instead of a perfectly square edge, there is a tail comprising charge that went through trapping/release during readout. CTE, in this respect, is calculated as follows:
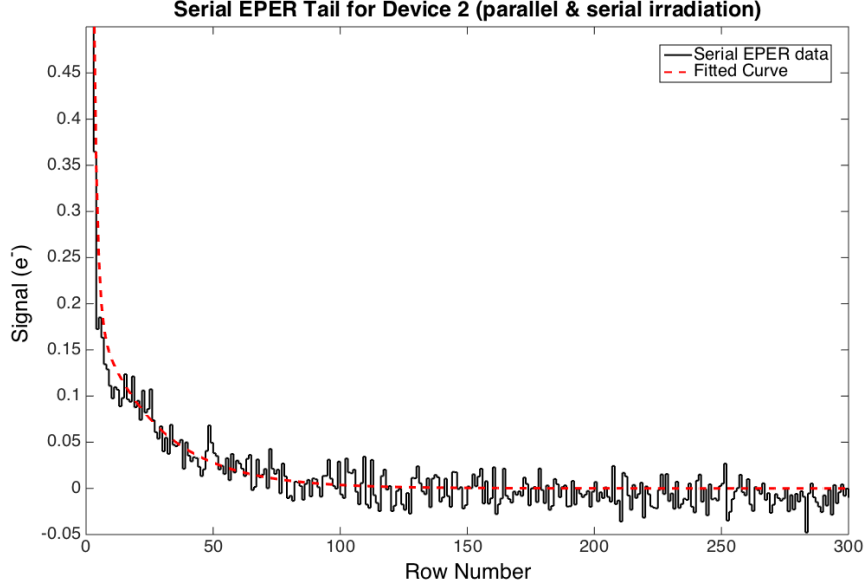
Figure 18. Serial EPER tail for device 2 (parallel and serial irradiation), where as before, the first 300 pixels are shown. Here the deferred charge is much more obvious than the parallel measurement in the first ∼100 pixels or so, likely due to probing different trap species at the different clock timings.

$$CTE = 1 - \frac{S_D}{S_{LC}(e^-) \cdot N_P}, \tag{11}$$

where S_D is the deferred charge, S_{LC} is the charge in the last column read out, and N_P is the number of pixel transfers.

Importantly, we note that the signal collected with each pixel passes through the conventional and EM registers before the output, therefore the serial CTI represents a combination of CTI from both. By only using the EPER method, it is not possible to separate these components. The measured low-level CTI is expected to be worse than the x-ray CTI method, and this should be considered when interpreting the EPER results. As before, CTE = 1 – CTI and we show results for CTE due to the charge deferred in the trailing 300 pixels following the flat field exposure of ∼8 e⁻, see Figs. 17 and 18.

As shown in Table 9, parallel CTI for devices 1 and 2, preirradiation, agrees within the error budget and are of order 10^{-4}. We measure degradation of a factor of ∼5 postirradiation. We cannot fully assess the effect of serial CTI, which appears to degrade by a much smaller factor than parallel CTI. This could mean that serial CTI in the context of this experiment was dominated by the EM register as a result of higher operating voltages and interaction with surface states based on the operating conditions that were used for this particular measurement.

6.5 Significance of Results for the WFIRST-CGI

The results from the phase I radiation study are encouraging when comparing the BOL and EOL detector performance relative to the requirements for the CGI. Based on current models that predict planetary yield as function of integration time, the most dominant sources of noise, or the performance parameters of the device that we must pay particular attention to, are dark current, CIC, and CTI. After annealing that followed the phase I radiation testing, we can report that the CCD201 measured dark current at operational temperatures of -108° C (IMO) passes the CGI requirement both before and after a DDD of 2.5×10^9 protons cm⁻², reflecting an EOL dose in L2 for 10 mm of tantalum shielding. Running at this temperature may affect the CTI under high-gain conditions, and these effects are discussed in the material that follows. Moreover, we can report no measurable increase in CIC within measurement error for pre- and postirradiation of both the parallel section or the serial register for this unbiased, room temperature irradiation under phase I. The results of CTI are still being

considered, and the operating conditions of the device will play a vital role for optimization. In the following material, we outline the "lessons learned" from the phase I study, as well as the phase II study that commenced in June 2015.

6.5.1 Lessons learned from phase I

The phase I experimental setup used standard CCD201 operating voltages and bias conditions as provided by the e2v CCD201 specifications sheet. The phase II testing began in June 2015 and is outlined in Sec. 6.5.2. This study will greatly benefit from "lessons learned" directly from phase I results, where the information can be applied in a way that will optimize the control electronics to maximize performance for all important device parameters. Any recommendations for optimization from phases I and II will be applied directly to the CGI strategy in achieving the required S/N.

- **Multiplication Gain:** We found that the $R\phi2HV$ and ϕDC parameters can have a strong effect on the CTI of the gain register of the device. Based on an operating temperature of -108° C (165 K), running the $R\phi2HV$ clock with lower voltages can maintain better charge transfer; however, this is likely temperature dependent. Furthermore, a lower setting in ϕDC can result in a higher gain for the same $R\phi2HV$ since the difference between these two parameters will define the gain. If this is set too low, serial CTI can increase.

- **Dark Current:** Having prior knowledge of a specific device's pinning potential, V_{SPP}, prior to irradiation would be beneficial. Currently, the projected CGI operating mode will be in IMO due to greater suppression of surface dark current. In IMO, V_{SS} is raised to a point where the semiconductorinsulator interface is subjected to large populations of holes that subsequently capture electrons, thereby suppressing surface traps from emitting such charge. We found that if $V_{SS} > V_{SPP}$, the parallel CIC may be affected, where there will be a tradeoff between dark current and CIC in this case. Measurements of dark current and CIC as a function of V_{SS} may elucidate this potential optimization.

- **Parallel & Serial CIC:** Clock amplitudes and precision timings in the controller are essential to minimizing the contribution of CIC. Indeed, the CCCP controller is highly tuned in this respect. As expected, for the electronics used during phase I, we observed that operating at lower clock amplitudes and faster speeds reduced the CIC in both the parallel and serial sections. However, much like dark current and CIC re: V_{SS}, there is a tradeoff with CIC and CTI re: clock amplitudes and timing. Multilevel clocking techniques have shown promising results in minimizing CTI while reducing CIC.[53] Importantly, by combining multilevel clocking with a design modification (as outlined in Secs. 5.5.4 and 5.5.6), one can increase the parallel CIC to negligible levels with reduced CTI. This work is ongoing and will be considered for the WFIRST-CGI.

- **CTI:** These subsections have already outlined useful optimizations for charge transfer. As noted previously, by adjusting many of these operating parameters, there is likely a tradeoff between one performance criteria and another, e.g., CIC/CTI or CIC/dark current. Once optimized for flight at BOL, the primary concern for degradation of charge transfer, characterized by CTI, will be the capture and emission time constants for different trap species within the buried channel, coupled with the device operating temperature. Furthermore, different EMCCD modes, such as photon-counting or analog mode, may be affected in different ways, where one mode may be recommended earlier in the mission under less damage, than another. Such trap properties are vital when considering clock speeds and other clocking parameters, in addition to wave shapes and operating temperature. Optimization of these parameters is ongoing at JPL where different design recommendations will be put forward based on the accrued damage from BOL and EOL.

6.5.2 Phase II irradiation plan

The phase II irradiation study took place at the Helios-3 beamline in Harwell, United Kingdom, and was the first of its kind for the CCD201 for the reasons outlined in the following material. This new plan commenced on June 01, 2015, and consisted of:

1) A preirradiation characterization of two science-grade CCD201s.

2) Four separate irradiation and characterizations at the following proton fluences: 1.0×10^9, 2.5×10^9, 5.0×10^9 and 7.5×10^9 protons cm^{-2} that reflect the full range of radiation doses that a sensor would undergo during a 6-year flight in L2, by considering both tantalum and aluminum shielding of varied thicknesses (see Fig. 6).

3) During the irradiation process at Harwell, the sensor was maintained at a temperature of -108° C (165 K) for all fluences and was kept at this temperature during characterization in order to avoid annealing the effects of damage. A vacuum chamber has been designed to operate in the Harwell beamline for this reason.[60]

4) The CCD was powered on during irradiation in order to investigate a positive flat-band shift as is expected in flight.

5) Post-irradiation characterization of each sensor.

Subsequent analysis of the radiation-damaged sensors at JPL will further reveal the effects of annealing on the device following characterization at Harwell. Additionally, thermal cycling testing will also be carried out.

By assessing the sensor's radiation damage at a consistent cryogenic temperature, the density of defects and populations of the various trap species are expected to be different when compared to a room temperature irradiation, subsequently impacting dark current and CTI. We believe that this study, coupled with what was learned from phase I, will be an accurate representation of what an EMCCD will undergo in orbit by considering the effects of displacement damage. The operating modes mirrored the phase I setup, with the exception of some of the modifications that were outlined in Sec. 6.5.1. For example:

- The read noise was measured by using the CCD201's 16 prescan elements that are located adjacent to the high gain output, see Fig. 3. In this test, the high voltage clock was powered down as opposed to back-clocking the register, resulting in no signal in this region and a clean measure of the read noise from the output amplifier.

- The multiplication gain was measured only when it has reached a stable condition, by using a customized sequencer that has been developed at the CEI. By passing large amounts of signal through the EM register prior to full testing, the multiplication gain can be accurately measured since this prevents any transient effects that may impact the Rϕ2HV clock at the beginning of a read out sequence, e.g., thermal stability of electronics.

The primary proton beam energy at Harwell is 7.5 MeV, with a flux of $\sim 1.0 \times 10^7$ protons cm^{-2} sec^{-1}. Much like PSI, the dosimetry is expected to be <10% across the full sensor area. Because the primary beam is of energy <13.5 MeV, the NIEL equations [refer to Eqs. (6)–(9)] used previously will differ:

$$\text{10 MeV NIEL Function} = \frac{8}{E_p^{0.9}}, \tag{12}$$

where E_p is the primary beam energy (MeV), yielding a total fluence of 1.92×10^9 protons cm^{-2} sec^{-1}. Furthermore, it is possible that some equipment may become activated by the primary beam. Since this equipment may be radioactive as a result, postirradiation only commenced once the surrounding conditions were safe for personnel and to avoid additional signal in the images. Prior to irradiation, an engineering grade device has undergone activation tests to assess the stability of defects in the device (e.g., dark current), so that a plan is in place postirradiation to assess the effects of annealing if necessary.

Thermal cycling at JPL. After initial postcharacterization has been completed at the CEI, the irradiated science-grade CCD201s will be shipped to JPL where they will undergo multiple thermal cycles over the projected mission survival temperature range. Furthermore, each device will undergo a thermal soak at >50° C and at -120° C for 24 h for survival testing. Automated testing will be designed and implemented in order to do so. Full device characterization will be carried out post-thermal soak, paying particular attention to the effects of annealing.

7. CONCLUSIONS

Here, we present performance characterization of the CCD201- 20 EMCCD that has been baselined for the WFIRST-CGI. This characterization has been carried out for BOL conditions, as well as conditions that reflect the space environment of the CGI at the EOL of a 6-year flight in L2, specifically, displacement damage due to protons assuming a 10-mm tantalum shield. In the case of BOL characterization to meet the CGI detector requirements, we use the Nüvü Cameras EMN2 camera system with the CCCP controller, which uses highly tuned clocking to achieve subelectron read noise, dark current of order 5×10^{-4} e$^-$ pix $^{-1}$ sec^{-1} at -85° C in IMO, and CIC of order 10^{-3} e$^-$ pix $^{-1}$ fr^{-1}. The measurement of initial radiation-induced performance degradation was carried out at the PSI in Switzerland using generic drive electronics from XCAM Ltd., and parameters, such as multiplication gain, dark current, CIC and CTI, were assessed, as well as their impact on the CGI application. We report degradation of dark current of a factor of ∼1.8, which still meets CGI requirements for a temperature of -108° C at EOL. Similarly, no degradation of CIC was observed following room temperature irradiation, and we are still assessing the effect of charge transfer degradation of a factor of ∼1.12 in the EM register and ∼5 in the parallel section. The phase I study has provided important information on the required operating parameters in order to minimize dark current, CIC and CTI, as well as highlighting trade-offs between voltage/bias conditions and precision timing of an EMCCD controller, in order to provide the best overall SN performance for the WFIRST-CGI. A second phase of the radiation study commenced in June 2015 and was completed in August 2015, which was the first of its kind for a CCD201-20. The device was irradiated over the full range of proton fluences reflecting BOL to EOL for L2 that reflect realistic conditions of the WFIRST-CGI EMCCD sensors, while kept at cryogenic temperatures where the device was under power to measure flat-band shifts as expected in flight. These results will be released following subsequent analysis.

ACKNOWLEDGMENTS

REFERENCES

1. D. Spergel, N. Gehrels, C. Baltay, et al., "Wide-Field InfrarRed Survey Telescope-Astrophysics Focused Telescope Assets WFIRST-AFTA 2015 Report," *arXiv150303757S*, 2015.
2. Q. Gong, et al., "Prototype Imaging Spectrograph for Coronagraphic Exoplanet Studies (PISCES) for WFIRST/AFTA," Proc. SPIE, 9605, 96050G (2015).
3. V. S. Dhillon, M. J. Stevenson, D. C. Atkinson, et al., 2007, MNRAS, 378, 825.
4. D. Ives, N. Bezawada, V. Dhillon, et al., 2008, Proceedings of SPIE., 7021.
5. N. M. Law, S. T. Hodgkin, and C. D. Mackay, 2006, MNRAS, 368, 1917.
6. M. Matuszewski, C. Daphne, R. M. Crabill, et al., 2010, Proceedings of SPIE., 7735.
7. D. O'Donoghue, 1995, Balt. Astron., 4, 517.
8. R. J. Stover, and S. L. Allen, 1987, PASP, 99, 877.
9. J. C. Wilson, S. S. Eikenberry, C. P. Henderson, et al., 2003, Proceedings of SPIE., 4841, 451.
10. B. J. Rauscher, D. Alexander, C. K. Brambora, et al., "Detector arrays for the James Webb Space Telescope near-infrared spectrograph," *Society of Photo-Optical Instrumentation Engineers (SPIE) Conference Series*, **6690**, 2007.

11. J. Beletic, R. Blank, D. Gulbransen, et al., "Teledyne Imaging Sensors: infrared imaging technologies for astronomy and civil space," *Society of Photo-Optical Instrumentation Engineers (SPIE) Conference Series*, **7021**, 2008.

12. R. Blank, S. Anglin, J. W. Beletic, et al., "H2RG focal plane array and camera performance update," *Society of Photo-Optical Instrumentation Engineers (SPIE) Conference Series*, **8453**, 2012.

13. P. Jerram, P. J. Pool, R. B. et al., "The llccd: low-light imaging without the need for an intensifier," in *Sensors and Camera Systems for Scientific, Industrial, and Digital Photography Applications II*, *Proc. SPIE* **4306**, pp. 178–186, 2001.

14. J. Hynecek, "Impactron - A New Solid State Image Intensifier", *IEEE Trans. on Electron Devices*, **48**, 10, 2001

15. Y. Bai, W. Tennant, S. Anglin, et al., "4K×4K format 10 μm pixel pitch H4RG-10 hybrid CMOS silicon visible focal plane array for space astronomy," *Society of Photo-Optical Instrumentation Engineers (SPIE) Conference Series*, **8453**, 2012.

16. R. A. Gaume, and B. N. Dorland, "The Joint Milli-Arcsecond Pathfinder Survey: Introduction and Applications", in *AIAA SPACE Conference & Exposition*, **6458**, 2009.

17. H. Michaelis, T. Behnke, S. Mottola, et al., "Investigations on performance of Electron Multiplied CCD detectors (EMCCDs) after radiation for observation of low light star-like objects in scientific space missions," *Proc. SPIE Sensors, Systems, and Next-Generation Satellites XVII*, **8889**, 2013.

18. R. Kohley, P. Garé, C. Vétel, et al., "Gaia's FPA: sampling the sky in silicon", *Society of Photo-Optical Instrumentation Engineers (SPIE) Conference Series*, **8442**, 2012.

19. J. Endicott, S. Darby, S. Bowring, et al., "Charge-Coupled Devices for the ESA Euclid M-class Mission", *High Energy, Optical, and Infrared Detectors for Astronomy V*, **8453**, 04, 2012.

20. R. Kimble & WFC3 Team, "In-flight Performance of the Detectors on HST/Wide Field Camera 3", *Detectors for Astronomy/European Southern Agency, 12-16 Oct. 2009; Garching; Germany*, **20090031927**, 2009.

21. T. Prod'homme, A. G. A. Brown, L. Lindegren, et al., "Electrode level Monte Carlo model of radiation damage effects on astronomical CCDs", *MNRAS*, **414**, 2215, 2011.

22. J. R. Janesick, "Scientific charge-coupled devices," in *SPIE Optical Engineering Press*, **xvi 906**, 2001.

23. D. J. Hall, N. J. Murray, A. D Holland, et al., "Determination of in situ trap properties in CCDs using a "single-trap pumping" technique," *IEEE Transactions on Nuclear Science*, **61**, pp. 1826-1833, 2014.

24. D. J. Hall, N. J. Murray, J. P. D. Gow, et al., "Studying defects in the silicon lattice using CCDs," *Journal of Instrumentation*, **9(12)**, article no. C12004, 2014.

25. D. J. Hall, N. J. Murray, J. P. D. Gow, et al., "In situ trap parameter studies in CCDs for space applications," *In: High Energy, Optical, and Infrared Detectors for Astronomy VI*, **22-27 June**, 2014.

26. D. Wood, D. Hall, N. Murray, et al., "Studying charge-trapping defects within the silicon lattice of a p-channel CCD using a single-trap "pumping" technique," *Journal of Instrumentation*, **9**, article no. C12028, 2014.

27. N. J. Murray, D. J. Burt, A. D. Holland, et al., "The relationship between pumped traps and signal loss in buried channel CCDs," *In UV/Optical/IR Space Telescopes and Instruments: Innovative Technologies and Concepts VI*, **25-26 August**, 2013.

28. N. J. Murray, A. D. Holland, J. P. D. Gow, et al., "Mitigating radiation-induced charge transfer inefficiency in full-frame CCD applications by 'pumping' traps," *In High Energy, Optical, and Infrared Detectors for Astronomy V*, **1-6th July**, 2012.

29. J. P. D. Gow, N. Murray, A. Holland, et al., "Assessment of space proton radiation-induced charge transfer inefficiency in the CCD204 for the Euclid space observatory," *Journal of Instrumentation*, **7**, C01030, 2012.

30. R. Massey, T. Schrabback, O. Cordes, et al., "An improved model of charge transfer inefficiency and correction algorithm for the Hubble Space Telescope," *MNRAS*, **439**, 887, 2014.

31. O. Daigle, J. L. Gach, C. Guillaume, et al., "CCCP: a ccd controller for counting photons," in *Society of Photo-Optical Instrumentation Engineers (SPIE) Conference Series*, *Proc. SPIE* **7014**, p. 6, 2008.

32. M. S. Robbins and B. J. Hadwin, "The noise performance of electron multiplying charge coupled devices," in *IEEE*, *Proc. IEEE* **50**, pp. 1227–1232, 2003.

33. J. L. Gach, C. Carignan, O. Hernandez. et al., "Development of a 4kx4k frame transfer electron multiplying ccd for scientific applications," in *Society of Photo-Optical Instrumentation Engineers (SPIE) Conference Series*, **9154**, 2014.

34. http://www.e2v-us.com/products/imaging/qe-curves/.

35. J. L. Barth, C. J. Isaacs, and C. Poivey, "The Radiation Environment for the James Webb Space Telescope," *JWST Document JWST-RPT-000453*, 2003.

36. T. M. Jordan, "NOVICE: A Radiation Transport/Shielding Code, Experimental and Mathematical Physics Consultation", $1983 - 2006$.

37. D. Burt, J. Endicott, P. Jerram, et al., "Improving radiation tolerance in e2v CCD sensors," in *Proc. SPIE*, **7439**, 2009.

38. D. J. Hall, A. D Holland, N. J. Murray, et al., "Modelling charge transfer in a radiation damaged Charge Coupled Device for Euclid," *In: High Energy, Optical, and Infrared Detectors for Astronomy V*, **Proc. of SPIE**, **8453**, 2012.

39. W. Shockley, and W. T. Jr. Read, "Statistics of the Recombinations of Holes and Electrons," *Physical Review*, **87(5)**, pp. 835-842, 1952.

40. H. Israel, R. Massey, T. Prod'homme, et al., **in prep**, *private communication*.

41. B. Dryer, D. Hall, "RVS Radiation Campaign 4 data I-III", *Data Calibration. GAIA*, 2014.

42. F. W. Sexton, et al., "Signal Event Gate Rupture in this gate oxides," *IEEE Trans. Nucl. Sci.*, **44**, 1262, 1997.

43. A. M. Evagora, N. J. Murray, A. D. Holland, and D. Burt, "Signal Event Gate Rupture in EMCCD Technology," *JINST*, **7**, C12002, 2012.

44. D. R. Smith, R. Ingley, A. D. Holland, "Proton Irradiation of EMCCDs," *IEEE Transactions on Electron Devices*, **53**, 2, 2006.

45. http://www.python.org.

46. http://proteus.space.noa.gr/ srem/herschel/.

47. http://www.nuvucameras.co-m/products.

48. www.e2v.com.

49. S. Seabroke, A. Holland, and M. Cropper, "Modelling radiation damage to ESA's Gaia satellite CCDs", *Proc. SPIE*, **7021**, 2008.

50. J. R. Janesick, "Photon Transfer DN - λ," in *Published by SPIE*, **ISBN 978-0-8194-6722-5**, 2007.

51. I. S. McLean, "Electronic Imaging in Astronomy," in *Praxis Publishing Ltd, Chichester*, **ISBN 978-3-540-76582-0**, 2008.

52. W. Maes, K. De Meyer, R. Van Overstraeten, "Impact ionization in silicon: a review and update", in *Solid State Electronics*, **6**, p. 705-718, 1990.

53. N. J. Murray, D. J. Burt, A. D. Holland, et al., "Multi-level parallel clocking of CCDs for: improving charge transfer efficiency, clearing persistence, clocked anti-blooming, and generating low-noise backgrounds for pumping," *UV/Optical/IR Space Telescopes and Instruments: Innovative Technologies and Concepts VI*, *Society of Photo-Optical Instrumentation Engineers*, **8860**, 2013.

54. O. Daigle, O. Djazovski, M. Francoeur, et al., "EMCCDs: 10 MHz and beyond," in *Society of Photo-Optical Instrumentation Engineers (SPIE) Conference Series*, *Proc. SPIE* **9154**, p. 6, 2014.

55. J. F. Ziegler, M. D. Ziegler, and J. P. Biersack, "SRIM the stopping and range of ions in matter,," *Nucl. Instrum. Methods Phys. Res., Sect. B*, **268(11–12)**, 1818–1823, 2010.

56. www.xcam.co.uk.

57. E. A. Burke, "Energy dependence of proton-induced displacement damage in silicon," *IEEE Trans. Nucl. Sci.*, **NS-33**, pp. 1276-81, 1986.

58. A. J. Van Lint, "The physics of radiation damage in particle detectors," *Nucl. Inst. Meth.*, **A253**, pp. 453-459, 1987.

59. J. R. Srour, C. J. Marshall, and P. W. Marshall, "Review of Displacement Damage Effects in Silicon Devices," *IEEE Trans. Nucl. Sci.,*, **50**, 3, 2003.

60. J. P. D. Gow, P. H. Smith, P. Pool, et al., "Proton Irradiation of a CCD236 Swept Charge Device at Cryogenic Temperature and the Subsequent Annealing," *Journal of Instrumentation*, **10**, C01037, 2015.